Effects of Heat Treatment and Irradiation on a Manganese-Stabilized Martensitic Stainless Steel

Robin Dawn Griffin

March 1990

UWFDM-825

Ph.D. thesis.

FUSION TECHNOLOGY INSTITUTE

UNIVERSITY OF WISCONSIN

MADISON WISCONSIN

Effects of Heat Treatment and Irradiation on a Manganese-Stabilized Martensitic Stainless Steel

Robin Dawn Griffin

Fusion Technology Institute
University of Wisconsin
1500 Engineering Drive
Madison, WI 53706

http://fti.neep.wisc.edu

March 1990

UWFDM-825

Ph.D. thesis.

EFFECTS OF HEAT TREATMENT AND IRRADIATION ON A MANGANESE-STABILIZED MARTENSITIC STAINLESS STEEL

by

ROBIN DAWN GRIFFIN

A thesis submitted in partial fulfillment of the
requirements for the degree of

Doctor of Philosophy
(Metallurgical Engineering)

at the
UNIVERSITY OF WISCONSIN-MADISON
1989

EFFECTS OF HEAT TREATMENT AND IRRADIATION ON A MANGANESE STABILIZED MARTENSITIC STAINLESS STEEL

Robin Dawn Griffin

Under the supervision of Professor R. Arthur Dodd

A recent requirement for materials which will be used in fusion reactors is that they have reduced long-life radioactivity. To reach this goal, nickel, molybdenum and niobium, common alloying elements used in steel, must be eliminated. In this research, a steel designed to meet these requirements has been studied. The steel has the composition 12% chromium, 6.5% manganese, 1% tungsten, 0.3% vanadium and 0.1% carbon (weight percent). It was designed to be fully air hardening.

The responses of the steel to tempering, aging, and irradiation were studied. It was tempered for two hours at 400°C, 500°C, 600°C, 700°C, 800°C, and 900°C for two hours, and for twenty-four hours at 500°C and 700°C. It was aged for 1000, 5000, and 10,000 hours at 365°C, 420°C, 520°C, and 600°C. Neutron irradiations at 420°C to 14, 47 and 114 dpa, at 520°C to 14 and 48 dpa, and at 600°C to 14 dpa were done. The steel was also irradiated with iron ions at 450°C, 550°C, and 650°C to 10, 20 and 40 dpa. At 550°C, the iron ions were co-implanted with helium ions to the level of 20 appm He/dpa.

The results showed that the steel had an A_{c1} which lay between 700°C and 800°C. $M_{23}C_6$ was the equilibrium carbide in the steel. The steel showed excellent resistance to swelling after irradiation. However, after

aging at 420°C and 520°C, and after neutron irradiation at 520°C, large amounts of an Fe-Cr-Mn-W chi phase formed. The results indicate that the addition of 6.5% manganese to 12% chromium, martensitic steels enhances chi phase formation. Its formation indicates that this steel may not be useful for fusion reactor applications.

Acknowledgements

I would like to thank Professors R.A. Dodd and G.L. Kulcinski for the privilege of working for them, and for their excellent advice. I also want to acknowledge Mr. Richard Casper for keeping the 200CX working, and for all the time he spent helping me. Daniel Pertzborn, David Plantz and Larry Seitzman, my friends and fellow group members have provided endless support and aid, and I deeply appreciate it. I also would like to thank the Fusion Technology Institute staff, Dennis Bruggink, Pat Caliva, Elaine DuCharme and Linda Kraft, for their help.

I must acknowledge the help of a number of people outside the University of Wisconsin. I want to thank Dr. David Gelles for his advice, for turning L9 over to me and for making PNL fun. Dr. Steven Zinkle, made it possible for the ion irradiations to be done at Oak Ridge National Laboratory, and I appreciate it. I also must acknowledge Dr. Frank Garner and the Northwest Colleges Association for Science (NORCUS) for providing the support for this research.

Finally, I want to thank my husband and family for all their support.

Table of Contents

List of Tables

List of Figures

Chapter 1: Introduction

Materials used in a fusion reactor will have to function in a severe environment. They will be exposed to a high neutron fluence, the production of helium by transmutation reactions, and possibly a corrosive coolant. A more recent goal of the world fusion materials community has been to develop alloys which also have reduced long-life radioactivity.

In the Deuterium-Tritium fusion fuel cycle, tritium is bred via the reactions

$$n + {}^{6}Li \rightarrow T + {}^{4}He$$

and

$$n + {}^{7}Li \rightarrow n + T + {}^{4}He.$$

The fusion reaction which provides neutrons to drive the above reaction is

$$D + T \rightarrow n + {}^{4}He + 17.6\ MeV.$$

In these reactions tritium is radioactive, but its half-life is only 12.3 years (1) so that unlike fission power, the fuel used in proposed fusion reactors will not have long-life radioactivity. The other source of radioactivity in fusion reactors will be that produced by interactions between the neutrons and the reactor material. The Nuclear Regulatory Committee regulation 10CFR61 contains the current rules on the handling of radioactive waste and Table 1 gives a brief description of the current nuclear waste classification and storage following the U.S. Nuclear Regulatory Commission guidelines (2).

Table 1.1: Nuclear Waste Classification and Storage Under Proposed 10 CFR Part 61 Rules

Waste Class	Definition	Disposal
Class A, segregated	Decays to acceptable levels during site occupancy	
Class B, Stable	Decays within 100 years to levels not dangerous to public health and safety.	Covered to reduce surface radiation to a few percent of background.
Class C, intruder	Decays to acceptably safe levels in more than 100 years but less than 500 years.	At least 5m below the surface, with natural or engineered barriers
Waste not meeting Class C, intruder waste definition.	Decays in more than 500 years.	Does not qualify for near surface disposal, proposed methods will be considered on a case-by-case basis.

The three methods available for limiting the activation of the materials used in a reactor are 1) material or elemental selection 2) isotopic tailoring and 3) dilution. The required dilution to make waste from a fusion reactor 'acceptable' could range from ten to several thousand (2). Isotopic tailoring has been considered in depth (2), but it would require the start-up of an entirely new industry to produce the material. The technique, designed for the separation of uranium isotopes, can be used on other elements. It also has the capability of removing elemental impurities.

Material and elemental selection are the major emphasis of current research. There are a number of materials being considered as structural materials in fusion reactors. Ceramics (e.g. SiC) have the potential for very low activation. Unfortunately, the normal impurities found in them would have to be removed as their presence essentially eliminates their low activation potential. Their high temperature capabilities would also be excellent, but their brittle nature would require complete redesign of the reactor (3). Vanadium alloys could be considered as low activation alloys, with low swelling and good high temperature strengths (4), however, such alloys would need a reactor design in which exclusion of air or other reactive gases are guaranteed at any region where the temperature might exceed 300°C to 350°C, because of their high sensitivity to interstitial impurities and a tendency to form volatile oxides (5). Making transition joints to other materials could also cause problems (3).

Steels are currently considered the most likely material for structural materials, with both ferritic and austenitic steels being investigated. There is

interest in the ferritic steels as they exhibit excellent swelling resistance when compared to many austenitics. However, the ferritics have a ductile to brittle transition temperature which can increase dramatically when they are irradiated. As far as achieving reduced long-life activation, the best classification which a steel can reach is class C (1). Elemental substitution or isotopic tailoring must be used to achieve this. Many activation calculations for potential fusion reactors have been performed (6,7), but complications arise for several reasons: 1)The cross-section data bases being used in the calculations are not complete, 2) the results are device dependent for different reactor designs, 3) the composition limits vary between manufacturers, and 4) current waste regulations may be changed by the time fusion reactors come on line. For these reasons, the allowable composition limits are subject to change, but are still useful for setting guidelines in alloy design. Table 2 lists the elements which will need to be limited for a steel to reach class C waste (4). These limits are additive so that when the limit of any one is reached, no more of any of the remaining components are allowed. It is interesting to note that some common alloying elements in steel such as Ni , Nb and Mo, will be limited.

The current study is on a reduced long-life activation martensitic steel. Other alloys being studied are the bainitic, 2% Cr alloys patterned after the 2 1/4% Cr, 1% Mo steels; stabilized 12% Cr martensitic steels patterned after HT-9; and 7-9 %Cr martensitic steels (8). The alloy of interest for this study is labelled L9, a stabilized 12%Cr, martensitic stainless steel.

Table 1.2: Initial Concentration Level Restrictions (appm)

10CFR1 Waste Disposal Rules

10 years After Shutdown, 9 Mw-yr/m^2 exposure

Element	Limiting Radionucleide	Limit (appm) Class A	Class B	Class C
Nitrogen	^{14}C	365	*	3650
Oxygen	^{14}C	250,000	*	$>10^6$
Aluminum	^{26}Al	$>10^6$	$>10^6$	$>10^6$
Cobalt	^{63}Co	30	$>10^6$	$>10^6$
Copper	^{63}Ni	12	240	2400
Iron	^{55}Fe	350	10^6	$>10^6$
Nickel	^{63}Ni	100	2000	20,000
Manganese	^{54}Mn	5000	$>10^6$	$>10^6$
Niobium	^{94}Nb	0.1	*	1
Molybdenum	^{94}Nb	365	*	3650
Zirconium	^{90}Sr	400	$>10^6$	$>10^6$

* Not defined under 10CFR1 waste disposal rules.

References for Chapter 1

1. F.W. Wiffen and R.T. Santoro, in *Proceedings of the Topical Conference on Ferritic Alloys for Use in Nuclear Energy Technology*, AIME, New York, (1984) 195.

2. Nuclear Regulatory Commission, "Licensing Requirements for Land Disposal of Radioactive Waste", 10Cf Part 61 Fed. Regist. 47 (248), 65446-82 (1982).

3. J.D. Gordon, J.J. Thomsonn, and S.N. Suchard in *IEEE 10th Symposium on Fusion Engineering*, Philadelphia, Pa.

4. R.W. Conn, E.E. Bloom, J.W. Davis, R.E. Gold, R. Little, K.R, Schultz, D.L. Smith, and F.W. Wiffen, *Nucl. Tech./Fusion* 5 (1984) 291.

5. D. G. Doran and R.L. Klueh, *MRS Bulletin* XIV(7) (1989) 45.

6. F.M. Mann, *Fusion Tech.* 6 (1984) 273.

7. H. Y. Khater, M.E. Sawan, S.W. Lomperski, I.N. Sviatoslavsky, UWFDM-802, Presented at the *13th Symposium on Fusion Engineering*, Knoxville TN (1989).

8. D.S. Gelles, "Effects of Irradiation on Low Activation Ferritic Alloys, A Review" in *International Symposium: Reduced Activation Alloys for Fusion Service,* Andover, Mass. (1988).

Chapter 2: Radiation Damage

Neutron and Ion Irradiation Comparison

When a metal is irradiated with energetic particles with sufficient energy, an atom can be removed from its lattice site. This atom, called a primary knock-on (PKO) can continue the displacement process by knocking off other atoms which themselves can cause further damage. This damage process can lead to many consequences. The point defects generated by irradiation can cluster to form dislocation loops and voids. They can enhance diffusion and creep, and they can alter the phase stability of the material.

Different irradiating species cause damage in different ways. Neutrons are neutral so that they can only transfer energy by nuclear collisions. Their collision cross section is small so that they travel a long way into a material causing a homogeneous damage production. Ions can transfer energy by both nuclear and electronic collisions. Their energy transfer rate is a function of the energy of the charged particle, e.g. for higher energies, the transfer rate is lower. Charged particle irradiations therefore give a displacement rate which is dependent on depth of penetration into the solid.

To correlate the two damage mechanisms, the dpa unit (displacement per atom) is used. One dpa means that on average every atom is displaced from its original site once during the irradiation. Point defect recombination,

dose rate effects, and spatial rearrangement due to thermal assisted migration are not accounted for.

For neutron irradiations (1)

$$dpa = N_{dn}/N = \phi_n \int N_n(E)\sigma(E,T)\upsilon(T)dEdT$$

where N_{dn} = the average number of atoms displaced per unit volume per neutron, N = the atomic number density of the crystal, N_n = the fraction of neutrons with energy E, $\sigma(E,T)$ = the cross section for a neutron of energy E To produce a PKA of energy T, $\upsilon(T)$ = the total number of atoms displaced by the PKA of energy T, and ϕ_n = the total neutron fluence. For ion irradiations, the fraction of energy lost in nuclear collisions must be known. Lindhard et. al. (2-5) have developed a model for determining this fraction where the nuclear and electronic energy losses are treated separately and the atoms are randomly distributed. The nuclear energy loss is calculated at a projected depth, $S_D(x)$. The formula used to calculate the dpa at different depths from ion irradiations is (6)

$$dpa = \phi_i \kappa S_D(x)/2E_D N$$

where ϕ_i = the fluence of heavy ions (#/cm2), N = the atomic density of the target material, E_D = the displacement energy of the material (for iron 25 ev is commonly used (7)). The term κ is determined by a formulant involving the properties of the incident and struck particles but is usually assumed to be equal to 0.8.

Other artifacts from ion irradiations exist. The ions injected during the irradiation can suppress void swelling by providing increased recombination with vacancies (8-10). The increased damage rate characteristic of ion

irradiations also causes a temperature shift in the peak swelling at which void swelling occurs (11). A void swelling temperature peak occurs because at low temperatures the excess vacancy flux decreases due to increased matrix recombination caused by a low vacancy mobility, while at high temperatures thermal emission of vacancies from voids increases, decreasing swelling. With an increased dose rate, the peak swelling temperature increases. This occurs because as the dose rate is increased the ratio of thermally emitted to excess inflowing vacancies decreases because the flux of thermally emitted vacancies is determined by temperature only.

Void Swelling

One of the possible results of radiation damage in materials is the swelling of materials by the nucleation and growth of voids. In this section the theories covering void swelling are reviewed.

The earliest attempts to develop a void nucleation theory are based on classical nucleation theory. The nucleation is assumed to have three stages. First, there is an incubation time during which a subcritical cluster population of vacancies forms. Next, a nucleation period occurs during which a group of clusters grows beyond a critical size because of growth fluctuations. Finally, nucleation ends when new vacancies no longer aggregate to nucleate new voids, but instead are incorporated into the existing void nuclei.

One of the earliest classical nucleation attempts at modeling void formation was performed by Harkness and Li (12). Vacancy production was

estimated from the neutron flux and the cross section for point defect pair production. They included defect annihilation due to vacancy interstitial recombination, and migration to various sinks. The nucleation equation is an expression for void nucleation in the presence of a vacancy supersaturation only, so the the effects of interstitials, dissolved gas atoms and impurities are not accounted for. The following energy equations were derived:

$$\Delta G_n^\circ = -nkT\ln(c_v/c_v^e) + (4\pi)^{1/3}(3V)^{2/3}\Omega n^{2/3}$$

where c_v and c_v^e are the actual and equilibrium concentration of vacancies, Ω is the crystal vacuum surface free energy and V is the atomic volume. From this a steady state rate of nucleation was derived

$$J_k = Z\upsilon_k N_o \exp(-\Delta G_k^\circ/kT)$$

where 1/Z is the width of ΔG_n° at kT below the maximum; υ_k is the rate at which vacancies impinge on the critical nucleus and N_o is the number of atomic sites per unit volume. The steady state nucleation rate will not be established immediately after a rapid change in vacancy concentration but will lag by a time known as the incubation time τ, where τ is given by

$$\tau = (2Z\upsilon_k)^{-1}.$$

Many other theories of void nucleation using classical nucleation theory were also developed. Wiedersich and Katz (13-15) use classical nucleation theory by detailing the balance of fluxes into and out of void embryos. Their first paper attempts to include the competing effects of interstitials and vacancies on the size distribution of void embryos (13). In their next papers they further generalize the theory to include the effects of insoluble gas molecules on the nucleation rate (14) and the effect of mobile

He on void nucleation (15). In their latest void nucleation paper (16), nucleation is described as a simultaneous reaction of vacancies, interstitials and gas atoms with embryos of all sizes. For quantitative predictions of the void densities an arbitrary assumption of the critical nucleus size is made. Their theory predicts that at a fixed vacancy supersaturation, an increase in interstitial concentration decreases the void nucleation rate and increases the size of the critical nuclei.

One of the most prolific workers in the classical void nucleation field is K.C. Russell (17-25). His completed formulation is essentially presented in reference 20. Russell uses a continuum model in which the volume and surface energies of small clusters are calculated. The theory reduces to several subcases, the most important of which are 1) spontaneous void nucleation driven by inert gases 2) heterogeneous nucleation on metastable gas/vacancy clusters 3) heterogenous nucleation on clusters of nongaseous impurities 4) homogeneous nucleation with or without the assistance of mobile, surface active impurities. In later papers, the theory was modified first with a more realistic gas law (25) and later to conditions of continuous helium generation (21).

A recent classical nucleation paper investigates the effect of radiation induced segregation on nucleation (26). It is shown that segregation of impurities and major alloying elements to void embryos can change the nucleation rate by a combination of 1) altering the surface energy and 2) altering void bias by changing the lattice parameter and shear modulus around the void. Mechanism 2 effectively changes the ability of interstitials to

reach the embryo. The effect of including divacancies into the theory (27) is shown to increase the nucleation rate.

Other theories are also in use for modeling void nucleation. Classical nucleation theory assumes that the defect populations are steady state throughout nucleation so that the the nucleation rate is constant. Lanore (28) uses an extension of the Wiedersich-Katz theory. With a computer, the dynamic changes are followed to avoid the steady state assumption. A Monte Carlo simulation which records the individual atom positions is used. The calculation assumes that gas is necessary for void nucleation. Computer time problems limit the amount of crystal and the time of irradiation which can be simulated.

Chemical reaction rate equations are also used for void nucleation by several authors (29-30). Mayer and Brown (29) use the method of chemical kinetics with the simplification that all voids have the same average radius rather than a size distribution. They include both mono and divacancies, assume gas is necessary for void nucleation, and include the effect of the developing interstitial loop population, which was not included in the classical nucleation theory. With chemical rate equations they follow the nucleation and growth of voids throughout the irradiation time without the classical nucleation assumptions of a steady state or the conditions for the termination of nucleation. Wiedersich (30) also uses chemical reaction rate theory to model void nucleation. In his method, a steady state solution to the set of reaction-rate equations is developed. The effect of excess interstitials

and vacancies, gases, and reactions with divacancies and other mobile defect clusters are included.

Wehner and Wolfer (31) use an entirely different method to calculate void nucleation results. They were concerned with all previous theories. Classical nucleation theories assume that the subcritical cluster population has no direct influence on the critical void size and the nucleation barrier. The chemical reaction rate theories have to assume an arbitrary number of vacancies and gas atoms for a stable void and the Monte-Carlo approach does not allow the current void size distribution to affect later void size distributions. Wehner and Wolfer have developed a time-dependent theory which describes the evolution of the entire cluster population using a Fokker-Planck equation. This is solved by a path sum construction giving the point-defect concentrations at a given time which are then fed back in to calculate concentrations at later time.

Many void nucleation papers have included in their formulation the effects of gases. The conclusion of some authors is that void swelling can not develop without the presence of gases (29,31). Inert gases, such as He, can reduce the critical size for void nucleation by "pressurizing" the cavity embryos. This would mean that the helium generated by transmutations in fusion reactor materials can enhance swelling. Bimodal cavity size distributions often develop in materials that are irradiated with He present. The cavity embryos, i.e. bubbles, initially form which contain different numbers of He atoms. If the number is too low, the bubbles do not grow because the size is below that of the critical size for void nucleation. But

cavity embryos with higher He contents have a lower critical radius size, so that the bubbles are more likely to grow (32). The bubbles will eventually convert to voids. Inert gases should also increase the probability that a void embryo will continue to grow (16, 20). In his later papers, Russell considered the possibility of helium-assisted nucleation (20-22,25). Wiedersich and Katz also included the effect of helium in a later paper (15). Mayer and Brown's chemical reaction rate theory, assumes that nucleation cannot occur without gases present (29).

Evidence also shows that reactive gases can nucleate voids. Most explanations are based on the assumption that the reactive gases assist nucleation by decreasing the surface energy of the void surface (33-36). Recent work by Seitzman (37,38) calculates this decrease in surface energy when oxygen adsorbs to the void embryo surface in austenitic stainless steels and nickel.

Chemical reaction rate theory is used to model void growth. The real material is replaced with a homogenized effective medium where point defect generation and loss occur throughout. Harkness and Li first modelled growth this way (39) and Wiedersich (40) and Brailsford et. al. (41) further developed the theory. The theory has been extended to include diffusion or surface reaction control (43), gas effects (44,45), spatial arrangement and effective generation rate of point defects (46-50), and dose rate effects (51,52). The point defect concentrations are obtained by numerically integrating the reaction rate equations. These are used to give the void growth rate (53)

$$dr_v/dt = \{Z_v(r_v)d_v[C_v - C^e(r_v)] - Z_i(r_v)D_iC_i\}/r_v$$

where C_v is the bulk thermal vacancy concentration, $C^e(r_v)$ is the thermal vacancy concentration at a void of radius r_v, D_i is the diffusivity of interstitials, C_i is the concentration of interstitials and Z_v and Z_i are the capture efficiencies of the void for vacancies and interstitials respectively.

Radiation Metallurgy

Besides causing void nucleation and growth in a material, radiation can induce other important changes. Radiation induced segregation (RIS) can dramatically affect a material's properties. Local composition changes can alter void swelling (54), the existing precipitate morphology and distribution, and can induce phase formation in an undersaturated alloy. Most theories treat solute segregation to point defect sinks, but RIS can also occur where local point defect recombination is uneven (55). The two redistribution mechanisms which are modeled in irradiated metals are defect-solute complex migration and the inverse Kirkendall Effect.

Defect-solute migration occurs when a point defect and a solute atom are able to move together. Johnson and Lam (56,57) have developed a model to describe this type of segregation for impurity level solute concentrations. They calculate solute segregation to voids and to a foil surface in an fcc metal by solving a set of rate equations. Their results indicate that the interstitial defect mechanism is primarily responsible for RIS. The model predicts a segregation peak at intermediate temperatures (around 0.4 T_m). This segregation is expected to be especially important for

undersize solutes as studies indicate (58-61) that undersize solutes trap interstitials more strongly than oversize solutes (62). At low temperatures most of the vacancies and interstitials recombine. At higher temperatures, any solute concentration which builds up is relieved by diffusion. For a lower defect production rate, the segregation peak temperature shifts downward.

For concentrated alloys, the Johnson and Lam model no longer applies as point defects are not likely to be adjacent to only one solute atom. The model proposed for concentrated alloy systems is the inverse Kirkendall model. The Kirkendall effect (63) occurs when components of an alloy diffusing by exchange with point defects move at different rates. This leads to a net flux of point defects. An inverse Kirkendall effect can occur in irradiated metals. A point defect flux, for example excess vacancies
migrating toward sinks, can set up a corresponding solute flux. Vacancy fluxes set up solute movement in the direction opposite to their flux, while interstitial fluxes will set up solute movement in the same direction as the interstitial flow. Manning (64), Marwick (65), and Wiedersich et. al. (66) have developed models for concentrated binary alloys and Lam et.al. (67) extended it to ternaries.

The most recent RIS explanations combine both defect complexes and inverse Kirkendall effects. For a given set of physical parameters there is a crossover temperature where defect complex segregation switches over to inverse Kirkendall effects (62,68). Defect-solute interactions are less effective for high temperatures so while they can dominate at low

temperatures the inverse Kirkendall effect takes over when the temperature increases.

Radiation induced phase transformation (RIP) is another serious problem for materials being considered for fusion reactors. Radiation can enhance or inhibit phase formation, and it can alter the shape and distribution of phases already present. Radiation enhanced diffusion, RIS, radiation disordering, amorphization and precipitate dissolution can lead to RIP.

Radiation enhances diffusion by increasing the concentration of point defects which provide normal atom mobility (69,70). Equilibrium phases which form too slowly to be seen by normal thermal treatments may appear. At high temperatures, the normal thermally produced vacancy concentration overwhelms the radiation effects and radiation enhanced diffusion is not important. Diffusivity depends on the vacancy migration and formation energies. At intermediate temperatures the enhanced diffusion is important. Vacancies are lost mostly to sinks and the diffusivity varies with dislocation density. At lower temperatures vacancies are lost by recombination with interstitials so that the diffusivity depends on the vacancy migration energy (71).

Radiation induced segregation is another source of phase transformations. Several authors (72,73) have extended Johnson and Lam's segregation model (56,57) to include the possibility of heterogeneous precipitation at point defect sinks if the solubility limit is exceeded. This type of precipitation can only shift the phase diagram laterally (74).

Homogeneous nucleation caused by RIS has also been proposed (55,75). The normal cluster size distribution in a stable solid solution can be disturbed by excess point defects. The rate of defect addition to clusters will be increased, and if the clusters are defect traps and the solute flow is toward the clusters, then RIS may lead to homogeneous precipitation. Segregation may also cause the existing precipitate distribution to become uneven. Precipitates may be clumped at sinks such as grain boundaries and be denuded elsewhere. The compositions of the phase may also be altered as segregation to a precipitate surface changes the local equilibrium there.

Radiation disordering (76,77) and amorphization (78) are also possible effects caused by the irradiating flux. Precipitate dissolution, another possibility, is modeled by Nelson et.al. (79). In this model, a particle loses solute by recoil at a rate proportional to its surface area. This solute is assumed to be evenly distributed around the precipitate. Solute then diffuses back and causes the precipitate to grow at a rate proportional to its radius. Wilkes (80) explicitly includes diffusion of solute in a cell around the particle and considers the possibility of new small particles nucleating around the original precipitate. Frost and Russell (81) calculate a steady state solute concentration in the matrix and the time it takes to reach it. Their model includes normal thermal coarsening. The calculation gives several possible results. For low damage rates and high temperatures, it predicts normal thermal coarsening. For low temperatures and high dose rates the precipitates present could totally dissolve. An intermediate possibility is

inverse coarsening where the small particles grow at the expense of the larger ones until they are all the same size.

The point defects formed during irradiation can affect the phases which are present. The results are calculated where vacancies are considered an additional alloying component (82) and their effect on free energy curves is considered (83). However, there are not enough point defects formed during irradiation to account for new phase formation (84,85). Another model proposed is the chemical vacancy effect (86). Excess vacancies can either stabilize or destabilize an incoherent precipitate. If δ is defined as

$$\delta = \{a_o(p) - a_o(m)\}/a_o(m)$$

where $a_o(p)$ is the lattice parameter of the precipitate and $a_o(m)$ is the lattice parameter of the matrix, then an oversize precipitate ($\delta>0$), would be stabilized by the increased vacancy arrival rate seen during irradiation. An undersized precipitate ($\delta<0$) would be destabilized.

Radiation Damage in Ferritic and Martensitic Steels

The microstructural trends in irradiated ferritic and martensitic steels are reviewed by Odette (87). He finds:

1) The swelling temperature range in ferritics is more narrow than that in austenitics. The peak swelling temperature is also lower. For neutron irradiations the peak swelling temperatures in ferritics is approximately 425°C, while for austenitics it occurs around 625°C. For ion and electron

irradiations the peak swelling temperature is 100°C to 150°C higher than in neutron irradiations (104). The swelling rate in ferritics (0.1%/dpa) is lower than that of austenitics (1.0%/dpa).

2) Helium promotes void formation and a bimodal distribution of helium bubbles and voids form. This will be a major problem in fusion reactors where the He (appm)/dpa ratio at the first wall is calculated to be 12. In the current fast reactors this ratio is only 0.12 (88).

3) Phase instabilities are likely to occur during irradiation.

4) The commercial martensitic alloy's subgrain structure may coarsen under irradiation.

One other tendency not mentioned by Odette is the tendency for the ferritic steels to increase the ductile to brittle transition temperature (89-91).

A number of reasons exist which explain the resistance of ferritic and martensitic steels to void swelling. Sniegowski and Wolfer (92) suggest that the difference in swelling resistance between austenitic and ferritic steels originates from the difference between their net biases. The relaxation volumes in ferrite and austenite are not equal. The interstitial relaxation volume for fcc alloys is almost twice that for bcc's and the reverse is true for the vacancy relaxation volumes. Using these facts, they calculate that the net bias for the fcc case is large while that for the bcc case is small.

Bullough et. al. (93) have developed another possible explanation for the swelling resistance of ferritic and martensitic steels. Two requirements are necessary for void growth. The first is a presence of sinks biased toward interstitials. The second is a presence of relatively neutral sinks. Analytical

expressions indicate that the magnitude of the bias to a dislocation increases with a larger Burgers vector (94-95). The model suggests that interstitial loop nucleation occurs before void nucleation and a small number of loops with a high bias for interstitials are surrounded by those with a relatively neutral network. The relatively neutral loops act as vacancy sinks and absorb the net vacancy flux created by the growth by preferential interstitial capture of the isolated high bias loops so that void nucleation is suppressed. This cannot explain all ferritic and martensitic resistance to swelling as it is still low in the temperature regimes where loops are not observed.

Little (96) suggests that both interstitial and substitutional solutes induce enhanced mutual recombination of point defects to decrease swelling. Point defect/solute trapping in ferritic and martensitic steel is possible due to the anisotropic strain associated with the solutes.

Odette (87) suggests that the higher self-diffusion rates in ferritic and martensitic alloys decreases their swellings. He also suggests that swelling in ferritic alloys is lower because the helium generation rates in fast reactors for ferritic are lower than for austenitic alloys. However, ferritic and martensitic alloys also swell less than austenitic alloys when comparisons are made between charged particle irradiations where He generation does not enter into the picture.

References for Chapter 2

1. G.L. Kulcinski, J.J. Laider, D.G. Doran *Radiation Effects* 7 (1971) 195.

2. J.. Lindhard and M. Scharff, *Phys. Rev.* 124(1) (1961) 128

3. J. Lindhard, M. Scharff, and H.E. Schiott, *Mat. Fys. Medd. Dan. Vid. Slesk,* 33(1) (1963).

4. J. Lindhard, V. Nielson, and M. Scharff, *Mat. Fys. Medd. Dan. Vid. Slesk,* 36(10) (1963).

5. H.E. Schiott, *Mat. Fys. Medd. Dan. Vid. Slesk* 35(9) (1966).

6. I. M. Torrens and M.T. Robinson in *Radiation-Induced Voids in Metals,* J.W. Corbett and L.C. Ianniello (Eds), USAEC Tech. Info. Center CONF-71061 (1972) 739.

7. J. Takamura, K. Furukawa, S. Miura, and P.H. Shingu, *J. Phys. Soc. Japan* 18 Supl. II (1963) 7.

8. A.D. Brailsford and L.K. Mansur, *J. of Nucl. Mat.* 71 (1977) 110.

9. F.A. Garner, *J. of Nucl. Mat.* 117 (1983) 177.

10. D.L. Plumpton, W.G. Wolfer, *J. of Nucl Mat.* 120 (1984) 245.

11. L.K. Mansur, *J. of Nucl. Mat.* 78 (1978) 156.

12. S.D. Harkness and C.Y. Li in *Radiation Damage in Reactor Materials Vol II.*, International Atomic Energy Agency, Vienna (1969).

13. J.L. Katz and H. Wiedersich, *J. of Chem. Phys.* 55(3) (1971) 1414.

14. J.L. Katz and H. Wiedersich, *J. of Nucl. Mat.* 46 (1973) 41.

15. H. Wiedersich, J.J. Burton, and J.L. Katz, *J. of Nucl. Mat.* 51 (1974) 287.

16. B.J.M. Loh, *Scripta Met.* 5 (1971) 841.

17. K.C. Russell, *Acta Met.* 19 (1971) 753.

18. K.C. Russell, *Scripta Met.* 6 (1972) 209.

19. R.W. Powell and K.C. Russell, *Rad. Effects* 12 (1972) 127.

20. K.C. Russell, *Acta Met.* 27 (1978) 1615.

21. C.A. Parker and K.C. Russell, *J. of Nucl. Mat.* 119 (1983) 82.

22. K.C. Russell, *J. of Nucl. Mat.* 61 (1976) 33.

23. S.I. Maydet and K.C. Russell, *J. of Nucl. Mat.* 82 (1979) 271.

24 K.C. Russell, *Scripta Met.* 3 (1969) 313.

25. C.A. Parker and K.C. Russell, *Scripta Met.* 15 (1981) 643.

26. A. Si-Ahmed and W.G. Wolfe, in *Effects of Radiation on Materials: Eleventh Conference*, ASTM-STP-782, H.R. Brager and J.S. Perrin, Eds., (1982) 1008.

27. W.G. Wolfer and A. Si-Ahmed, UWFDM-471 (1982).

28 J.M. Lanore *Rad. Effects* 22 (1974) 153.

29. R.M. Mayer, L.M. Brown, and U. Gosell, *J. of Nucl. Mat.* 95 (1980) 44.

30. H. Wiedersich, in *Consultant Symposium on the Physics of Irradiation Produced Voids*, R.S. Nelson, Ed., (1984) 147.

31. M. F, Wehner, W. G. Wolfer, *Phil. Mag. A* 52(2) (1985) 189.

32. L.K. Mansur and W.A> Goghlon *J. of Nucl. Mat.* 119 (1983) 1-25.

33. R. W. Ballufi and D. N. Seidman in *Proceedings of the Conference on Radiation Induced Voids in Metals,* Albany, NY (1972) 563.

34. K. Farrell, *Rad. Effects* 53 (1980) 175.

35. N.H. Packen and K. Farrell, *J. of Nucl. Mat.* 78 (1978) 143.

36. A.J.E. Foreman and B.N. Singh, in *Proceedings from Dimensional Stability and Mechanical Behavior of Irradiated Metals and Alloys*, Brighton, England, (1983) 95.

37. L.E. Seitzman, G.L. Kulcinski, and R.A. Dodd, in *Radiation-Induced Changes in Microstructure 13th Int. Symp.*, ASTM-STP-95, (1987) 279.

38. L.E. Seitzman, L. Wang, G.L. Kulcinski, and R.A. Dodd, *J. of Nucl. Mat.* 141 & 143 (1986) 738.

39. S.D. Harkness and C.Y. Li, *Met. Trans.* 2 (1971) 1457.

40. H. Wiedersich, *Rad. Effects* 12 (1972 111.

41. A.D. Brailsford and R. Bullough, *J. of Nucl. Mat.* 44 (1982) 121.

43. L.K. Mansur, P.R. Okamoto, A. Taylor, and C.Y. Li, *Nucl. Metall.* 18 (1973).

44. A.D. Brailsford and R. Bullough, in *Physical Metallurgy of Reactor Fuel Elements*, J.E. Harris and E.C. Sykes Eds., TMS (1973) 148.

45. G.R. Odette and S.C. Langley, in *Proceedings of the International Conference on Radiation Effects and Tritium Technology for Fusion Reactors*, CONF-750989 vol. I, US Energy Research and Devlopment Administration, Gatlinberg, Tennessee, (1975) 395.

46. J. R. Buler Jr., *Trans. Am. Nucl. Soc.* 27(1977) 314.

47. A.J.W. Foreman, *Rad. Effects* 21 (1974) 81.

48. J.L. Straalsund, *J. Nucl. Mat.* 51 (1974) 302.

49. R. Bullough, B.L. Eyere and K. Krishani, AERE-R7952, UK Atomic Energy Research Establishment, Harwell, England (1975).

50. D.G. Doran and J.O. Shiffgeens, in *Proc. Workshop on Correlation of Neutrons and Charged Particle Damage*, Oak Ridge National Laboratory, CONF-760673, U.S. Energy Research and Development Administration (1976) 3.

51. A.D. Brailsford and R. Bullough, *J. of Nucl. Mat.* 44 (1972) 121.

52. R. Bullough and R.C. Perrin, in *Irradiation Effects on Structural Alloys for Nuclear Reactor Applications*, ASTM-STP-484, ASTM (1970) 317.

53. L.K. Mansur, *Nucl. Tech.* 40 (1978) 5.

54. W.G. Wolfer, *J. of Nucl. Mat.* 114 (1983) 292.

55. R. Cauvin and G. Martin, *Phys. Rev. B* 23 (1981) 3322.

56. R.A. Johnson and N.Q. Lam, *Phys. Rev. B* 13(10) (1976) 4364.

57. R.A. Johnson and N.Q. Lam, *Phys. Rev. B* 15(4) (1977) 1794.

58. M.L. Swanson and L.M. Howe, *J. of Nucl. Mat.* 69&70 (1978) 176.

59. P.H. Oederichs, C. Lehman, H.R. Schober, A. Scholz, and R. Zeller, *J. of Nucl. Mat.* 69 & 70 (1978) 176.

60. L.E. Rehn, K.H. Robrock, and H. Jacques, *J. Phys. F: Metal Phys.* 8 (1978) 183T.

61. T.H. Blewitt, C. Surtain, T.L. Scott, and R.A. Corners, *Bull. Am. Phys. Soc.* 20 (1975) 296.

62. P.R. Okamoto and L.E. Rehn, *J. of Nucl. Mat.* 83 (1979) 2.

63. E.O. Kirkendall, *Trans. AIME* 147 (1942) 104.

64. J.R. Manning, *Bull. Am. Phys. Soc.* 23 (1978) 287.

65. A.D. Warwick, *J. of Phys. F: Metal Phys.* 8 (1978) 1849.

66. H. Wiedersich, P.R. Okamoto, and N.Q. Lam, *J. of Nucl. Mat.* 83 (1979)

67. N.Q. Lam, A. Kumar, and H. Wiedersich in *Effects of Radiation on Materials* ASTM-STP-782 (1982) 985.

68. P.R. Okamoto, L.E. Rehn, and R.S. Averback, *J. of Nucl. Mat.* 108&109 (1982) 319.

69. R. Sizmann, *J. of Nucl. Mat.* 69&70 (1978) 386.

70. Y. Adda, M. Beyeler, and G. Brebec, *Thin Solid Films* 25 (1975) 107.

71. J.A. Hudson, *J. Brit. Nucl. Energy Soc.* 14 (1975) 127.

72. N.Q. Lam, P.R. Okamoto, H. Wiedersich, and A. Taylor, *Met. Trans. A* 9 (1978) 1701.

73. G. Martin, *Phil. Mag. A* 38(2) (1978) 131.

64. K.C. Russell, *J. of Nucl. Mat.*, 83 (1979) 176.

75. G. Martin, R. Cauvin, J.L. Bocquet, and A. Barbu in *Phase Stability During Irradiation* J.R. Holland, L.K. Mansur, and D.I. Potter, Eds., AIME Pittsburgh, PA (1980).

76. FL.M. Howe and M.H. Rainville, *J. of Nucl. Mat.* 68 (1977) 215.

77. M.L. Jenkins, M. Wilkens, *Phil. Mag.* 34 (1976) 1155.

78. G.J.C. Carpenter and E.M. Schulson, *J. of Nucl. Mat.* 23 (1978) 180.

79. R.S. Nelson, J.A. Herdson, and D.J. Mazey, *J. of Nucl. Mat.* 44 (1972) 318.

80. P. Wilkes, *J. Nucl. Mat.* 83 (1979) 166.

81. H. J. Frost and K.C. Russell, *Acta Met.* 30 (1983) 953.

82. G. Martin, *Phil. Mag.* 32 (1975) 615.

83. P. Wilkes, K.Y. Liou, and R.A. Lott, *Rad. Effects* 29 (1976) 249.

84. J.L. Bocquet, G. Martin, *J. Nucl. Mater.* 83 (1979) 186.

85. P. Wilkes, *J. Nucl. Mater.* 83 (1979) 166.

86. S.I. Maydet, K.C. Russell, *J. Nucl. Mater.* 64 (1977) 101.

87. G.R. Odette, in *Fusion Reactor Materials Semiannual Progress Report*, DOE/ER-0313-3, (1988) 106.

88. G.R. Odette in *Damage Analysis Fundamental Studies Quarterly Progress Report*, DOE/ER-0046/21, (1985) 19.

89. F.A. Smidt Jr., J.R. Hawthorne, and V. Proniza in *Effects of Radiation on Materials* ASTM (1981) 269.

90. R.L. Klueh, J.M. Vitek, and M.L. Grossbeck *J. of Nucl . Mater.* 103&104, (1981) 887.

91. N.S. Cannon, W.L. Hu, and D.S. Gelles, in *Fusion Reactor Materials Semiannual Progress Report*, DOE/ER-0313/2 (1987) 119.

92. J.J. Sniegowski and W.G. Wolfer, UWFDM-535 (1985).

93. R. Bollough, M.H. Wood, and E.A. Little in *Effects of Irradiation on Materials*, ASTM-STP-725, ASTM (1981) 593.

94. A.D. Brailsford, R. Bullough, and M.R. Hayns, *J. Nucl. Mater.* 60 (1976) 246.

95. R. Bullough, M.R. Hayns and C.H. Woo, *J. Nucl. Mater.* 84 (1979) 93.

96. E.A. Little, *J. Nucl. Mater.* 87 (1979) 11.

Chapter 3: Martensitic Stainless Steels

Metallurgy of 12% Cr Martensitic Stainless Steels

Martensitic steels with chromium levels of 12% are of interest because of their "stainless" properties. Low carbon steels which contain 12% Cr, have the ferrite, pearlite and bainite transformations pushed back, so that the steel is air hardened (1). The steels are then alloyed for the following properties: 1) no delta ferrite at room temperature (for improved toughness), 2) tempering resistance, 3) a high temperature (A_{c1}) at which the martensite reverts to austenite (at least 700°C), 4) the M_f-the temperature at which martensite formation ends- at or above room temperature (to eliminate retained austenite) (1-3). The elements C, Ni, N, Mn, and Co are all austenite formers while Cr, Si, Mo, W, V, Al, Ti, and Nb are delta ferrite formers (2). The elements which are added to increase the tempering resistance of the steel are unfortunately also those elements which enhance delta ferrite formation. The addition of these elements must be offset with compensating austenite formers. The classic method of determining phase stability at room temperature is to use the Schaeffler diagram shown in Figure 3.1 (4). In this diagram, all elements are normalized to a Cr (delta ferrite former) or to a Ni (austenite former) equivalent. The equations for the Cr and Ni equivalents are

$$\text{Cr equivalent} = Cr + 2(Si) + 1.5(Mo) + 5(V) + 5.5(Al) + 1.75\,(Nb) + 1.5\,(Ti) + 0.75(W)$$

$$\text{Ni Equivalent} = Ni + Co + 0.5(Mn) + 0.3(Cu) + 25(N) + 30(C)$$

Carbon and nitrogen cannot be increased in a steel without causing some serious degradation in its properties. They both drastically reduce the steels weldability and impact resistance (3) and nitrogen has limited solubility and can lead to porosity in the ingots (2). Nb and Ti are strong carbide and nitride formers and thus increase the temperature needed to solution anneal. This can increase the prior austenite grain size which decreases the toughness of the steel (3). Care in alloying also has to be used as the change in elements affect the M_s (the temperature at which martensite formation begins), M_f and A_{c1} temperatures (4).

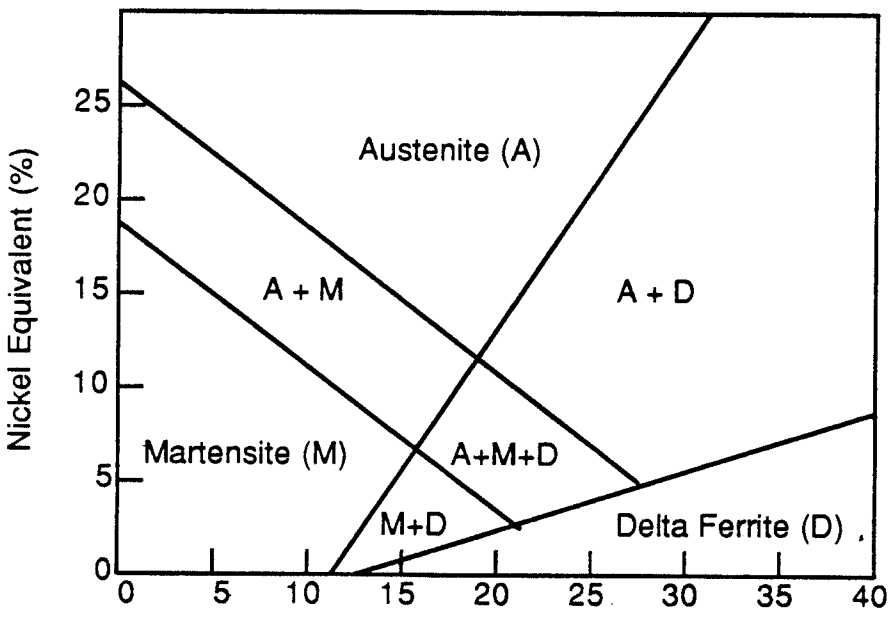

Figure 3.1. Shaeffler diagram for use in determining phase stability in stainless steels.

L9 Background

The composition of L9 and HT-9, the steel on which L9 is based, are shown in table 3.1 (5). Tempering resistancein HT-9 is obtained by the addition of Mo, but Mo is one of the restricted elements for low activation alloys as shown in table 1.2. Vanadium and tungsten are other possible alloying elements for tempering resistance and they are both used in L9. The carbon content is reduced to 0.1% for increased toughness, and Ni, another restricted alloying element, is eliminated. To compensate for the loss of these austenite stabilizers, manganese was added to eliminate the delta ferrite in the steel.

Table 3.1: Composition of L9 and HT-9 (wt %)

Alloy	Cr	C	V	W	Mn	Si	N	Ni	Mo
HT-9*	12	0.2	0.3	0.5	0.6	0.4	------	0.5	1.0
L9**	12	0.1	0.3	0.9	6.5	0.11	0.003	------	------

* Nominal Composition

** Measured Composition

Neutron irradiated results from L9 have been presented in a number of papers and reports. The samples were irradiated in the Fast Flux Test Facility (FFTF) Materials Open Test Assembly (MOTA) in Richland, Wa. In the studies, a series of TEM disks were irradiated at 420°C, 520°C and 600°C.

Miniature tensile specimens were irradiated at 420°C and 520°C, and Charpy samples were irradiated at 365°C. All samples first received the following austenitizing and tempering treatments: 1000°C/20 hr/AC to RT + 1100°C /10 min/AC to RT + 700°C/2 hr/AC to RT (AC = air cool, RT = room temperature). Table 3.2 shows the tensile test results for the unirradiated and irradiated alloy. It also includes tensile test results from unirradiated HT-9 (5-6).

The as-heat-treated tensile test results show a higher strength for L9 than HT-9 while the elongation of the two alloys remains comparable. The strength difference may be due to the heat treatment differences between the

Table 3.2: Room Temperature Tensile Test Results on L9 and HT-9

Alloy	Dose (dpa)	Nominal Irrad. T (°C)	Yield Strength (MPa)	Ultimate Strength (MPa)	Uniform Elongation (%)	Total Elongation (%)
HT-9	----------	----------	610	760	----------	12
L9	----------	----------	822	1002	2.3	10.1
L9	8.4	420	848	942	6.0	14.7
L9	43.7	420	684	853	9.3	16.1
L9	14.3	585	531	749	9.3	19.4
L9	37.2	585	449	744	18.0	21.2

steels. The 420°C, 8.4 dpa sample showed only moderate increases in strength while HT-9 significantly hardens during irradiation (5). Continued irradiation at 420°C to 44 dpa does not change the tensile test results significantly. The 585°C, 14.3 dpa tensile test results show considerable softening. The alloy softened more than HT-9 did when similarly irradiated (5). When the dose is increased to 37 dpa at 585°C, the tensile results do not indicate significant softening in L9.

Charpy impact test results at 365°C and 12 dpa show a large shift in the ductile to brittle transition temperature (DBTT) with a large change in the upper shelf energy. The unirradiated DBTT was -60° while the irradiated DBTT was 150°C (7). The unirradiated sample's brittle fracture mode is transgranular but that of the irradiated sample is along prior austenite grain boundaries (8).

Transmission electron microscopy results are also available for some of the irradiations (8,5,6). The unirradiated structure is the typical lath structure with an uneven distribution of $M_{23}C_6$.

In the 420°C, 8 dpa irradiations, an uneven distribution of a Cr rich α' forms. The hardening shown in the tensile test is not significant so α' does not seem to be causing significant problems. The 43 dpa structure is very similar. There are a few voids present and the dislocation structure has developed loops. At 114 dpa the void density was still very small indicating it is still in the incubation stage. The α' distribution is still nonuniform and remains stable with only minor coarsening (8). At 520°C and 14 dpa, the effects of irradiation are not as obvious. The precipitates have coarsened

and a few voids are present (5). Another phase, possibly either chi or Laves, is also seen. At 600°C, 34 dpa, portions of the martensite laths transform to more equiaxed subgrains. Carbides are coarsened and the unidentified precipitate is again present. Grains filled with stacking faults are also common following this irradiation. The structure of these grains may be austenite (8).

References for Chapter 3

1 K.J. Irvine, D.J. Crewe, and F.B. Pickering, *JISI* 195 (1960) 386.

2. E.A. Little, D.R. Harris, F.B. Pickering and S.R. Keown, *Metals Tech.* (1977) 205.

3. F.B. Pickering, *The 12 % Cr Steels Physical Metallurgy and the Design of Steels*, Applied Science Publishing Ltd., London (1978) 386.

4. H. Schneider, *Foundrey Trade J.* 108 (1960) 562.

5. D.S. Gelles and M.L. Hamilton, in *Alloy Development for Irradiation Performance Semiannual Progress Report*, DOE/ER-0045/13, (1985) 128.

6. D.S. Gelles and M.L. Hamilton, in *Alloy Development for Irradiation Performance Semiannual Progress Report*, DOE/ER-0045/16, (1986) 131.

7. N.S. Cannon, W.L. Hu, and D.S. Gelles, in *Fusion Reactor Materials Semiannual Progress Report*, DOE/ER-0313/2 (1987) 119.

8. D.S. Gelles and N.S. Cannon in the *International Symposium: Reduced Activation Alloys for Fusion Service*, Andover, Mass.(1988).

Chapter 4: Experimental Procedures

Heat Treatment Studies

The steel used in this study, was provided by Dr. D.S. Gelles of Battelle Pacific Northwest Laboratories. It came in the form of 500 μm thick sheet which had been cold rolled 50%. Two heat treatment studies were done on the steel. In the first, a series of short -time anneals were used to determine its tempering response. In the second, a set of long-time agings were used to characterize the steel's phase stability and thermal aging resistance. For both of these studies, the steel was first normalized at 1000°C for 20 hours and then air cooled to room temperature. To ensure precipitate dissolution, the steel was reheated to 1100°C for 10 minutes and again air cooled to room temperature.

The tempering study consisted of heating the steel to 400°C, 500°C, 600°C, 700°, 800°, and 900°C for two hours. Twenty-four hour tempers were also done at 500°C and 700°C.

To test the steel's aging response, transmission electron microscopy, (TEM), disks of the steel were aged for 1000, 5000, and 10,000 hours at 365°C, 420°C, 520°C, and 600°C after first tempering the steel for two hours at 700°C.

To determine if the normalized-only steel was fully martensitic, a step-scan on a Philips PW 1729 X-Ray Generator was done. Scans were done from 2θ = 48°-54° for the austenite (200) peak and from 2θ = 61°-69° for the

martensite (200) peak. At each 0.2°, counts were collected for 150 seconds. The amount of retained austenite was calculated with the method outlined by Erard (1).

Optical metallography and microhardness tests were also used to characterize the rolled, normalized-only, normalized + tempered, and the normalized + tempered + aged steel. The samples were polished to 0.05 μm alumina finish and then etched in Villella's reagent (5ml HCl, 1 g picric acid, 100 ml methanol) for approximately 20 seconds.

Transmission electron microscopy was also used to characterize the normalized-only, normalized + tempered, and normalized + tempered+ aged steel. TEM disks were jet-thinned in a solution of 10% perchloric acid and 90% butyl alcohol at -30°C in a Fischione twin jet electropolisher at 120V. Japanese Electron Optics Laboratory (JEOL) 100B and JEOL 200CX transmission electron microscopes (TEM) were used to characterize the samples. The JEOL 200CX was equipped with a Tracor Northern Energy Dispersive X-Ray (EDS) Spectrometer and a Scanning Transmission Electron Microscopy (STEM) unit. To make precipitate identification simpler, precipitates were extracted onto carbon films for examination in the TEM. Precipitates were extracted from the samples which were normalized + tempered , and from those which were normalized+tempered+aged. The tempered samples were first lightly etched in Villella's reagent to reveal the precipitate structure. A carbon film was evaporated onto the sample surface. The samples were again placed into Villella's reagent to etch off the precipitates with the carbon film attached. Finally, the films were suspended

on copper grids for examination in the TEM. Extraction from the aged samples was a little more difficult, as the samples were small TEM disks. These samples were also first lightly etched. A drop of 0.5% Formvar was put on their surfaces and allowed to dry, leaving a porous film on the surface. The samples were etched again to remove the precipitates, leaving them stuck to the Formvar film. Next, replicating tape was placed on the film and then stripped off so that the tape was left with a Formvar film and precipitates attached to it. A carbon film was evaporated onto this. The Formvar was dissolved in ethylene dichloride. The replicating tape was dissolved in an acetone evaporator leaving a carbon film with precipitates attached.

An Fe-Cr-Mn ternary was fabricated and aged to study the phase stability of the Fe-Cr-Mn system. The target composition of the alloy was 60%Fe, 25%Cr and 15% Mn. Before aging, the alloy was homogenized at 1250°C for 2 hours. It was rolled 11% and then 20% at 1000°C . It was then cold rolled 30%, 60%, 60%, 35% and 45% with each reduction followed by a solution anneal at 1030°C for 5 hours. Finally, the alloy was cold rolled 40% to a final thickness of 200μm, and punched into TEM disks. No solution anneal was done prior to aging. The disks were aged at 365°, 410° and 520°C for 2000 hours and at 520°C for 5000 hours. Optical metallography and transmission electron microscopy, (JEOL 200CX) were used to test the response of the alloy to aging.

Radiation Damage Studies

The TEM disks of the steel were irradiated in the Fast Flux Test Facility (FFTF), Materials Open Test Assembly (MOTA), in Richland Washington. The temperature during the irradiation was held to within ± 5°. The dose rate in the FFTF-MOTA is approximately $1x10^{-6}$ dpa/sec. Before irradiating the steel, it was given the normalizing and tempering treatment used in the aging study (1000°C/2 hr/AC to RT + 1100°C/10 min/AC to RT + 700°C/2 hr/AC to RT). Samples were irradiated to $3.1x10^{22}$ neutrons/cm^2 (≈ 14 dpa) at 595°C, they were irradiated at 520°C to $3.1x10^{22}$ neutrons/cm^2 and $1.0x10^{23}$ neutrons/cm^2 (≈ 14 and 48 dpa respectively), and they were irradiated at 420°C to $2.2x10^{22}$ (≈ 14 dpa), $9.5x10^{22}$ (≈ 43 dpa) and $2.6x10^{23}$ (≈ 114 dpa). Precipitates were extracted from the TEM disks after irradiation. These samples were characterized at Battelle Pacific Northwest Laboratories using a JEOL 100CX TEM equipped with a STEM unit and a Tracor-Northern EDS System.

The steel was ion-irradiated at the Oak Ridge National Laboratory's facility for heavy ion irradiation. The facility is equipped with two accelerators so that irradiation with both heavy and light-ions can be accomplished simultaneously (3). The 3.8 MeV Fe^{++} ions were accelerated with a vertical CN Van de Graff accelerator equipped with a Model 910 Physicon ion source. Figure 4.1 shows the displacement versus depth curve for 3.8 MeV Fe^{++} ions in iron which was calculated using the E-DEP-1 code (4). The He^{+}

were provided by a horizontal AN Van de Graaff accelerator. A uniform distribution of He^+ implantation was obtained by varying the accelerating voltage from 200-400kV. The region where Helium is implanted can be seen in Figure 4.1. Nine TEM disks can be loaded into the sample chamber for simultaneous irradiation. The dose rate was approximately $1x10^{-3}$ dpa/sec. The steel was irradiated at 450°C and 550°C with Fe^{++} ions only. The samples were back-thinned to 0.4 microns, to avoid surface and injected interstitial effects. Displacement levels at 0.4 μm of 8, 24 and 47 dpa were obtained at 450°C. At 650°C, the steel was irradiated to 6, 17, 30, and 40 dpa at 0.4μm. At 550°C, co-implantation with He^+ ions was used. Samples were irradiated to 6 dpa with 211 appm He at 0.4μm (35 appm He/dpa), to 18 dpa with 462 appm He (26 appm He/dpa), and to 40 dpa with 914 appm He (27 appm He/dpa).

The first 0.4 microns of the irradiated (and unirradiated) surface of the steel were removed by electropolishing for 38 seconds at 4 mA in a solution of 10% perchloric acid, 90% butyl alcohol at -50°C. The samples were then back-thinned by laquering off the irradiated surface and jet thinning in a solution of 10% perchloric acid and 90% acetic acid at 15°C, 65V. Investigation was done on the JEOL 200CX.

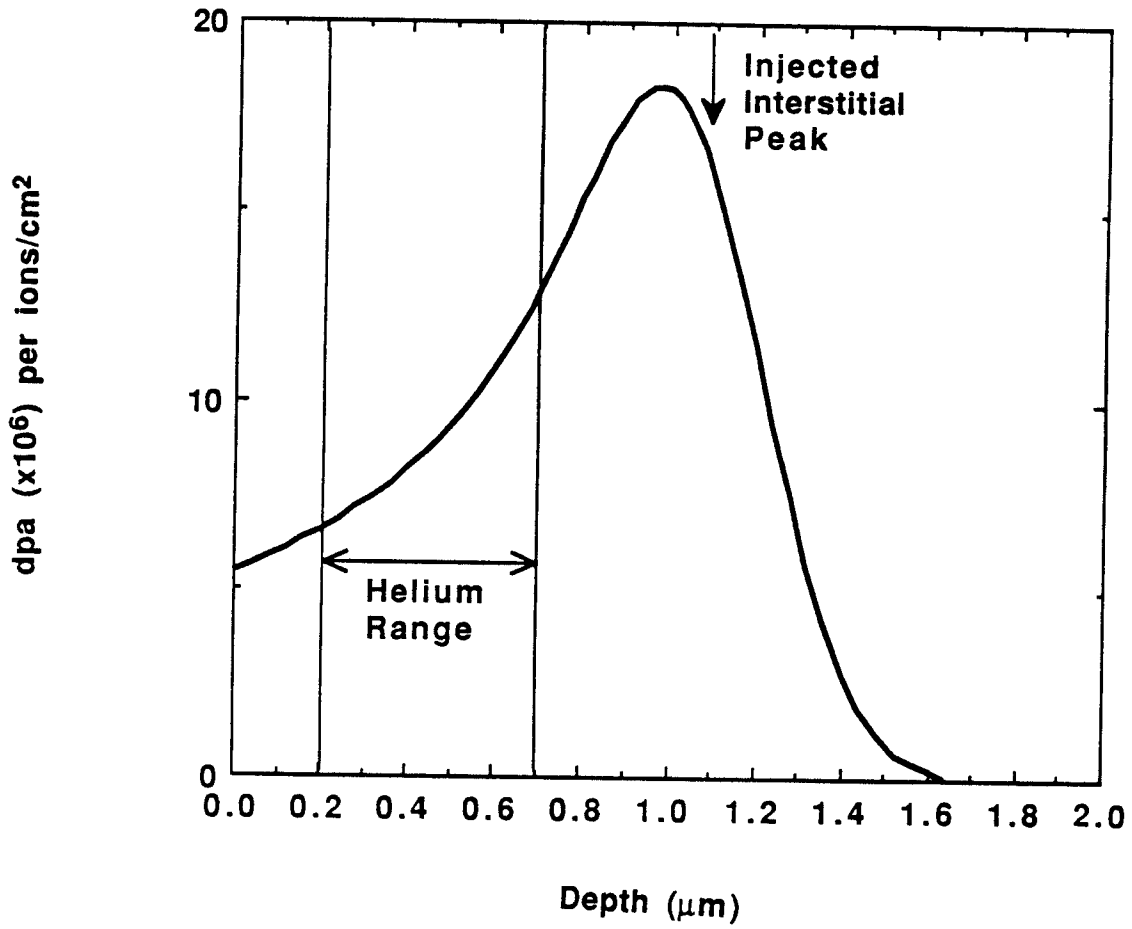

Figure 4.1. Displacement versus depth for 3.8 MeV Fe^{++} in iron.

References for Chapter 4

1. H. Robert Erarad in *Advances in X-Ray Analysis Vol. 7* , Eds. W.M. Mueller, G. Mallett, and M. Fay, Proceedings of the 12th Annual Conference on Applications of X-Ray Analysis, Plenum Press NY (1963) 256.

2. R. E. Bauer, *J. Nucl. Mater.* 103 & 104 (1981) 1563.

3. M. B. Lewis, N.H. Packan, G.F. Wells, and R.A. Buhl, *Nucl. Inst. Meth. 167* (1979) 233.

4. I. Manning and G.P. Mueller, *Comp. Phys. Commun.* 7 (1974) 85.

Chapter 5: Heat Treatment Results

Tempering Results

The structure of the normalized-only, and the normalized + tempered steel showed a fully martensitic structure as shown in the optical images of the rolled, normalized, and normalized + tempered steel (Figure 5.1). In many of the images, prior austenite grain boundaries are visible. The average size of these grains was 120 μm. The results of the x-ray diffraction step scan on the normalized only steel showed that there was some retained austenite after the normalizing treatment (Figure 5.2). The amount of retained austenite found in the steel was around 3% .

The Vickers microhardness results for the austenitized and tempered steel showed a sharp hardness drop when the steel was tempered between 500° and 700°C and then increased for tempering temperatures greater than 700°C (Figure 5.3).

The TEM images of the precipitates extracted from the tempered steel (Figure 5.4) showed that the precipitates which formed during the 400°C and 500°C two hour temper, were within the the martensite laths (Figure 5.4a,b). These precipitates were elongated multigrains and were identified as M_3C. Energy Dispersive X-ray (EDS) results showed the composition of the metal in the M_3C to be 65%Fe, 30%Cr and 5% Mn (weight percent). The precipitate showed the M_3C to form with its characteristic {110} habit plane

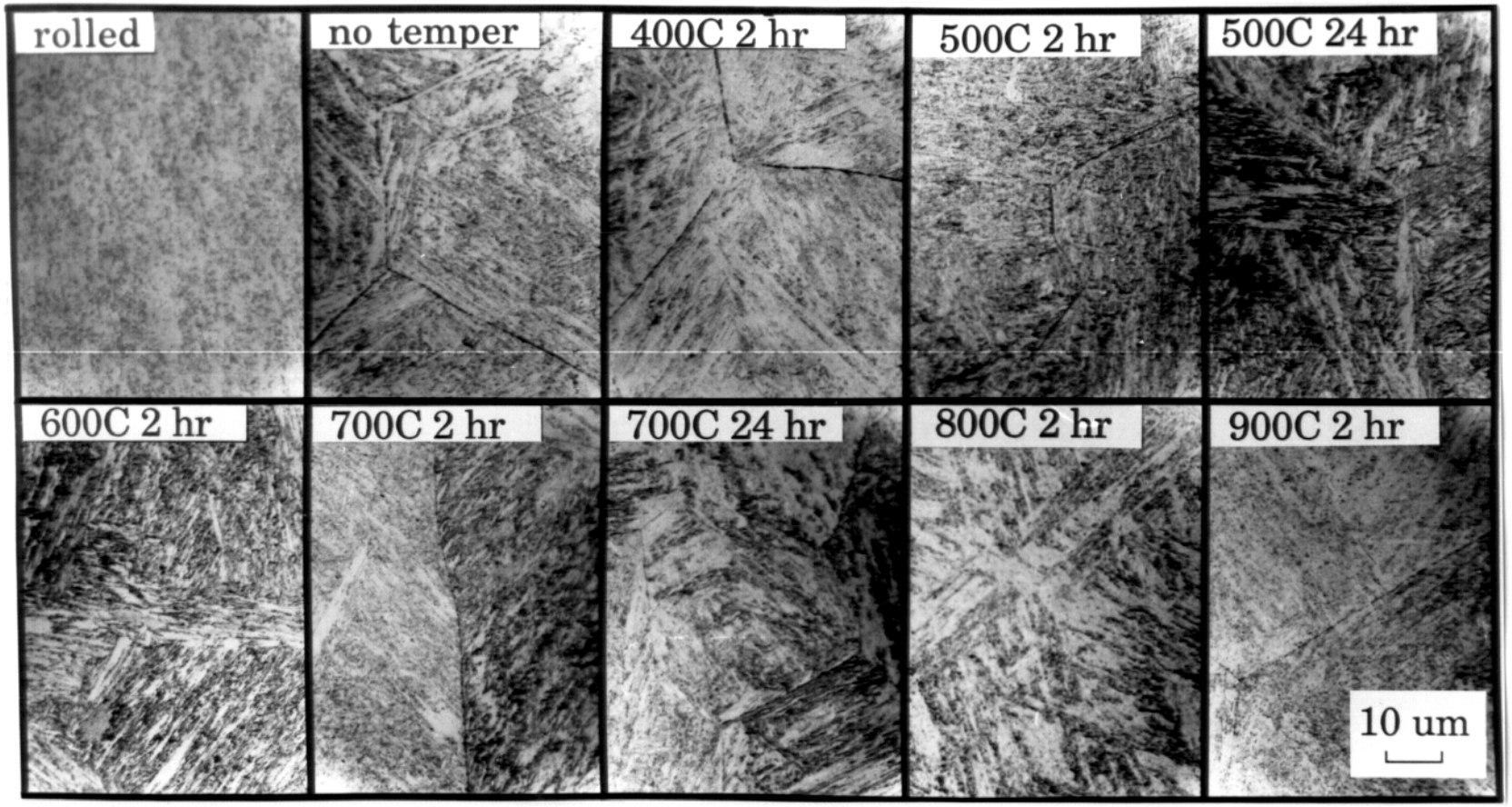

Figure 5.1. Optical metallography results from L9 in the rolled, normalized and normalized + tempered conditions.

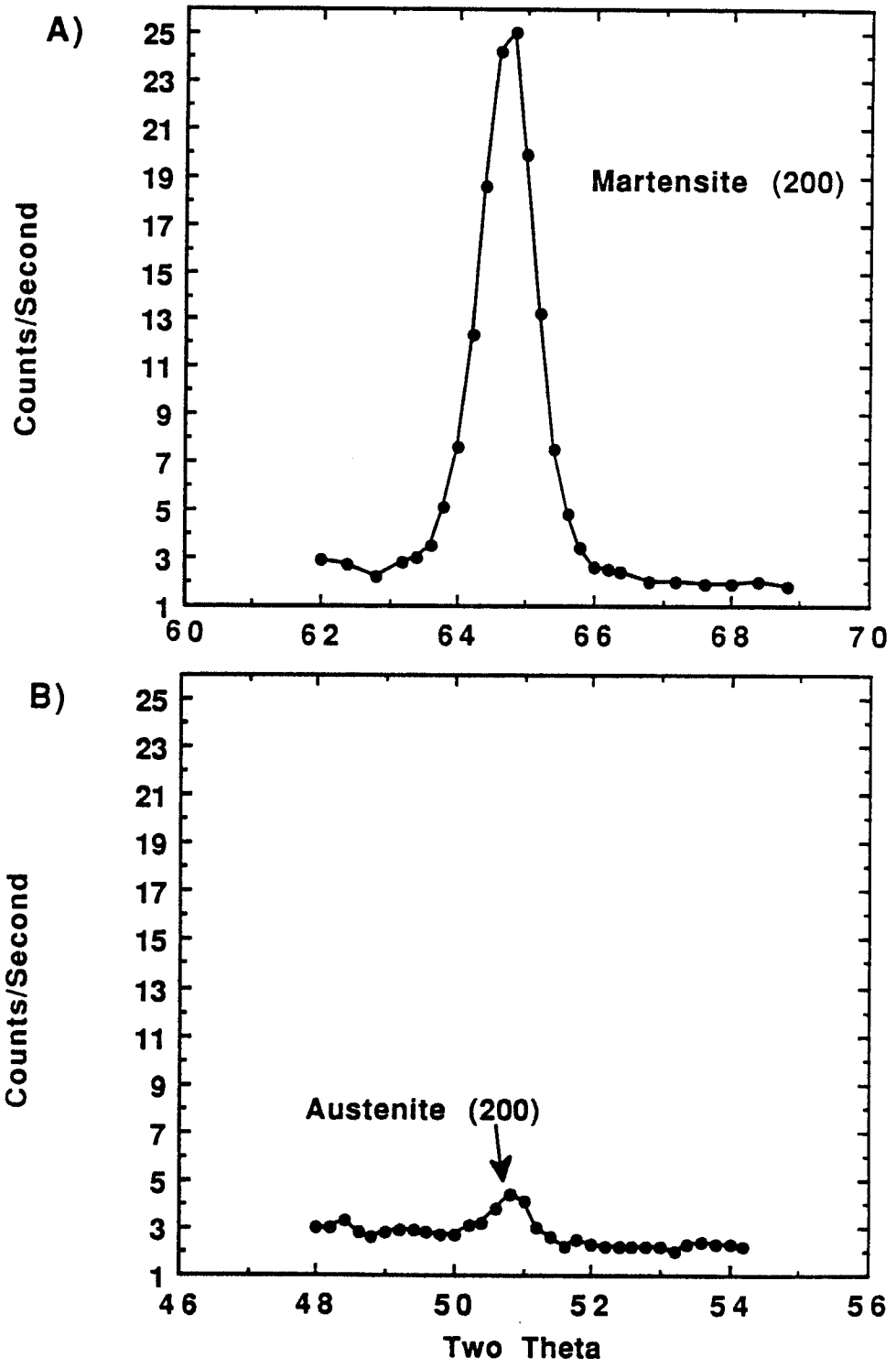

Figure 5.2. Austenite and martensite (200) peaks from normalized L9.

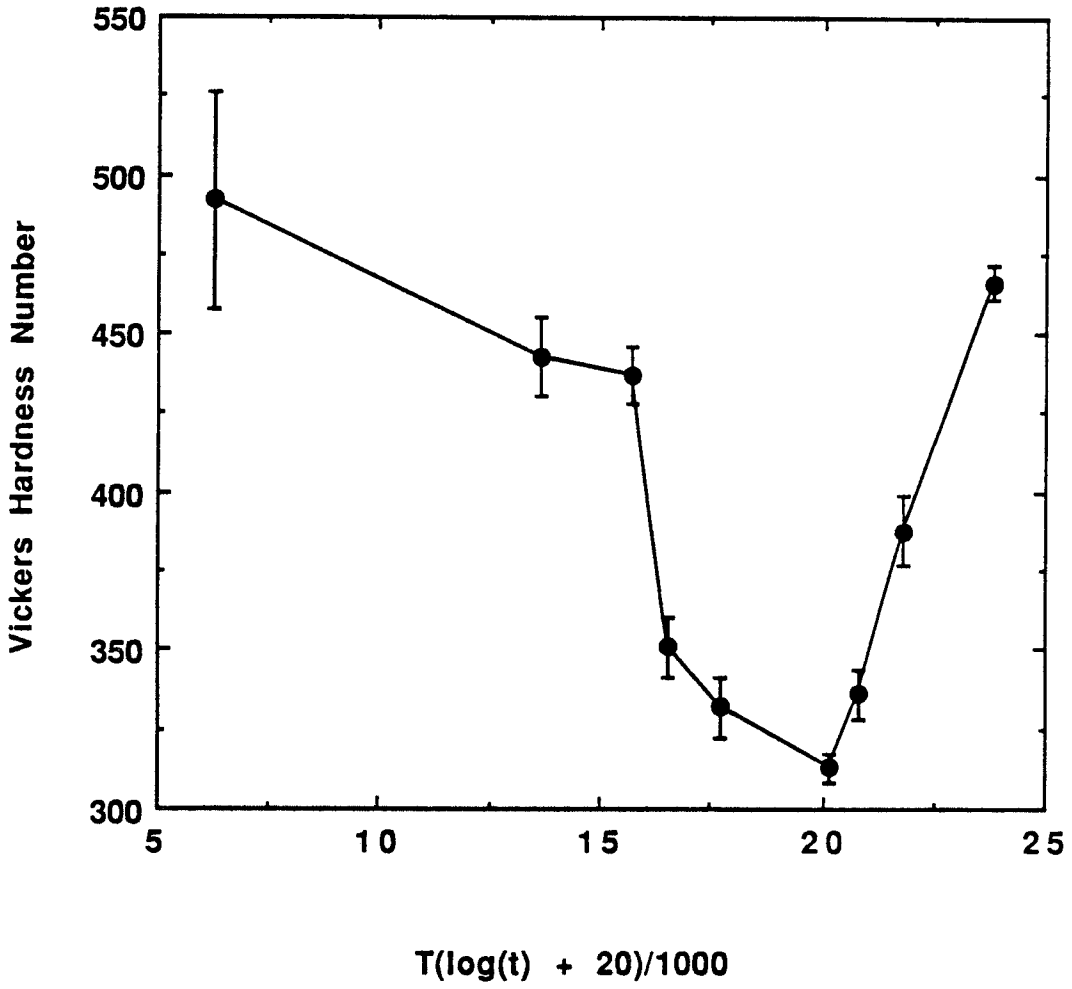

Figure 5.3. Microhardness results from normalized and normalized + tempered L9.

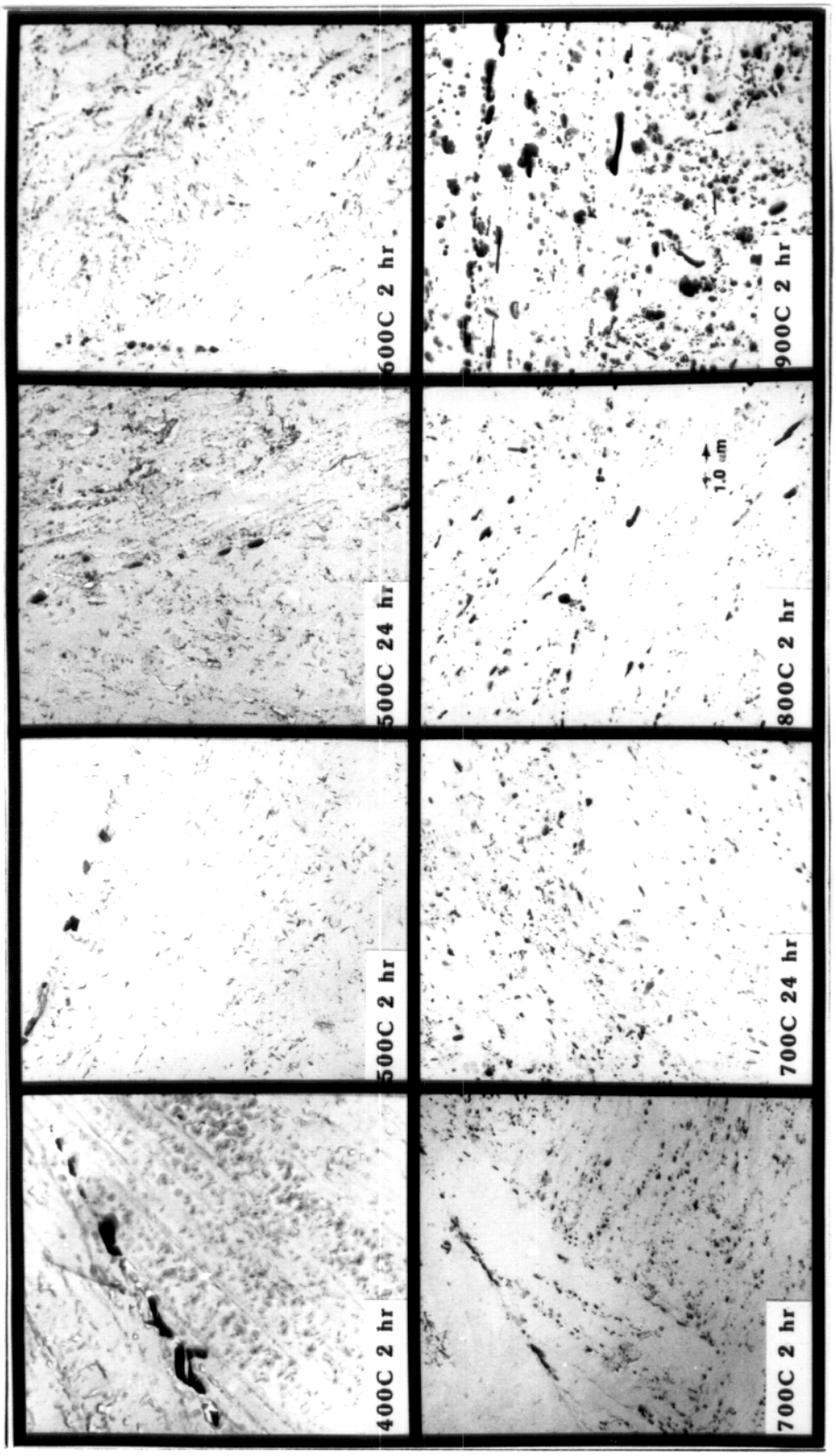

Figure 5.4. Precipitates extracted from normalized + tempered L9.

(1). In Figure 5.5, the TEM image shown is close to a (111) beam direction so that all three orientations of the M_3C are seen. The precipitates in the sample tempered for twenty four hours at 500°C were a mixture of M_3C and $M_{23}C_6$ (Figure 5.4c). The $M_{23}C_6$ tended to be single grain and the shape varied. At 600°C and higher, $M_{23}C_6$ was the only precipitate which was found (Figures 5.4d-h). Most of the images in Figure 4 contain prior austenite grain boundaries which were dotted with precipitates. At all the tempering temperatures the grain boundary precipitates were identified as $M_{23}C_6$. At 600°C and higher, there was a tendency for the $M_{23}C_6$ to lie on lath boundaries (Figure 5.6a). Using EDS, the composition of the metal in $M_{23}C_6$ was shown to be 58% Cr, 27% Fe, 10% W, 3% Mn and 2% V. Electron micro-diffraction results showed the fcc, a_o = 1.06 nm structure of $M_{23}C_6$ (Figures 5.6b and c), where a_o is the lattice parameter for $M_{23}C_6$.

Two types of inclusions were found scattered throughout the samples. First, MnS particles were found. These were large and round and were generally seen in groups (Figures 5.7a and b). Figures 5.7c and d are its electron micro-diffraction patterns. Figure 5.8a shows a TEM image of the second type of inclusion found, which has been identified as a spinel, an oxide seen in the steel when it was tempered at temperatures above 500°C. This image shows the typical rectangular shape of the phase. The metal composition of the phase was found to be 5.5% Al, 4.5% Ti, 2.4% V, 45.4%Cr, and 42.2% Mn. The small amounts of titanium and aluminum in the oxide must have originated during the fabrication of the steel and were probably not uniformly distributed as they were not seen in the vendor's

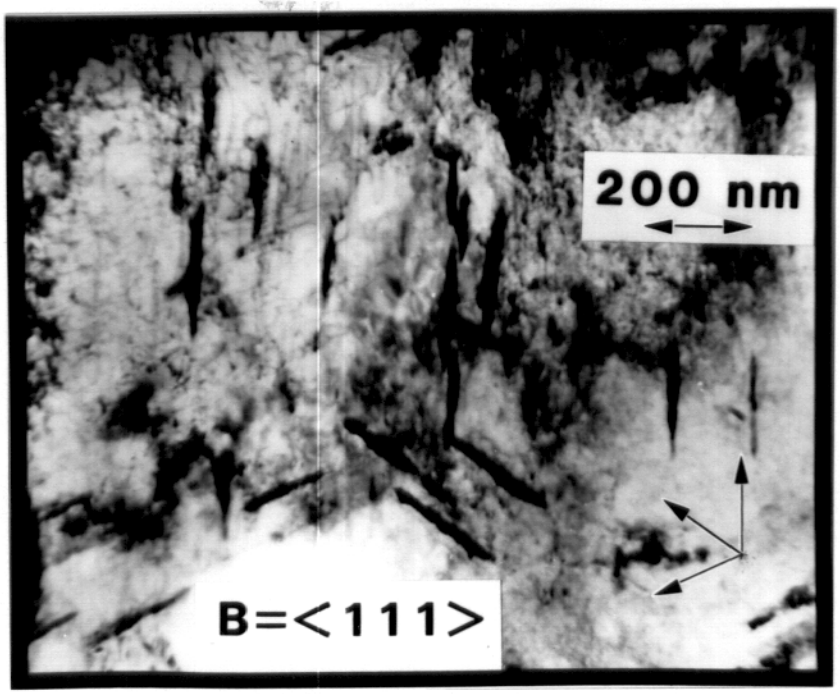

Figure 5.5. M_3C in tempered L9. Foil orientation is close to a (111), so that all three orientations are visible.

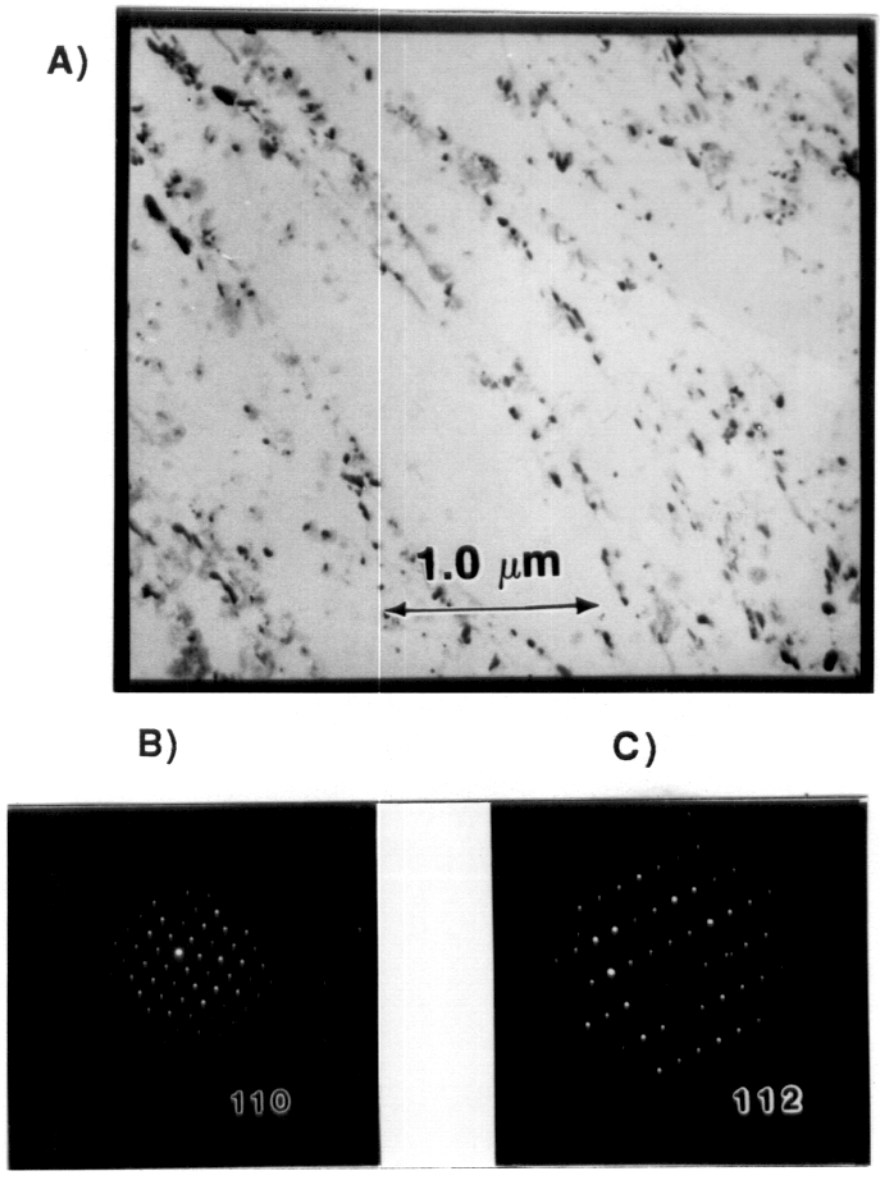

Figure 5.6. a) $M_{23}C_6$ precipitates extracted from L9 tempered for two hours at 600C. b and c) Microdiffraction from $M_{23}C_6$.

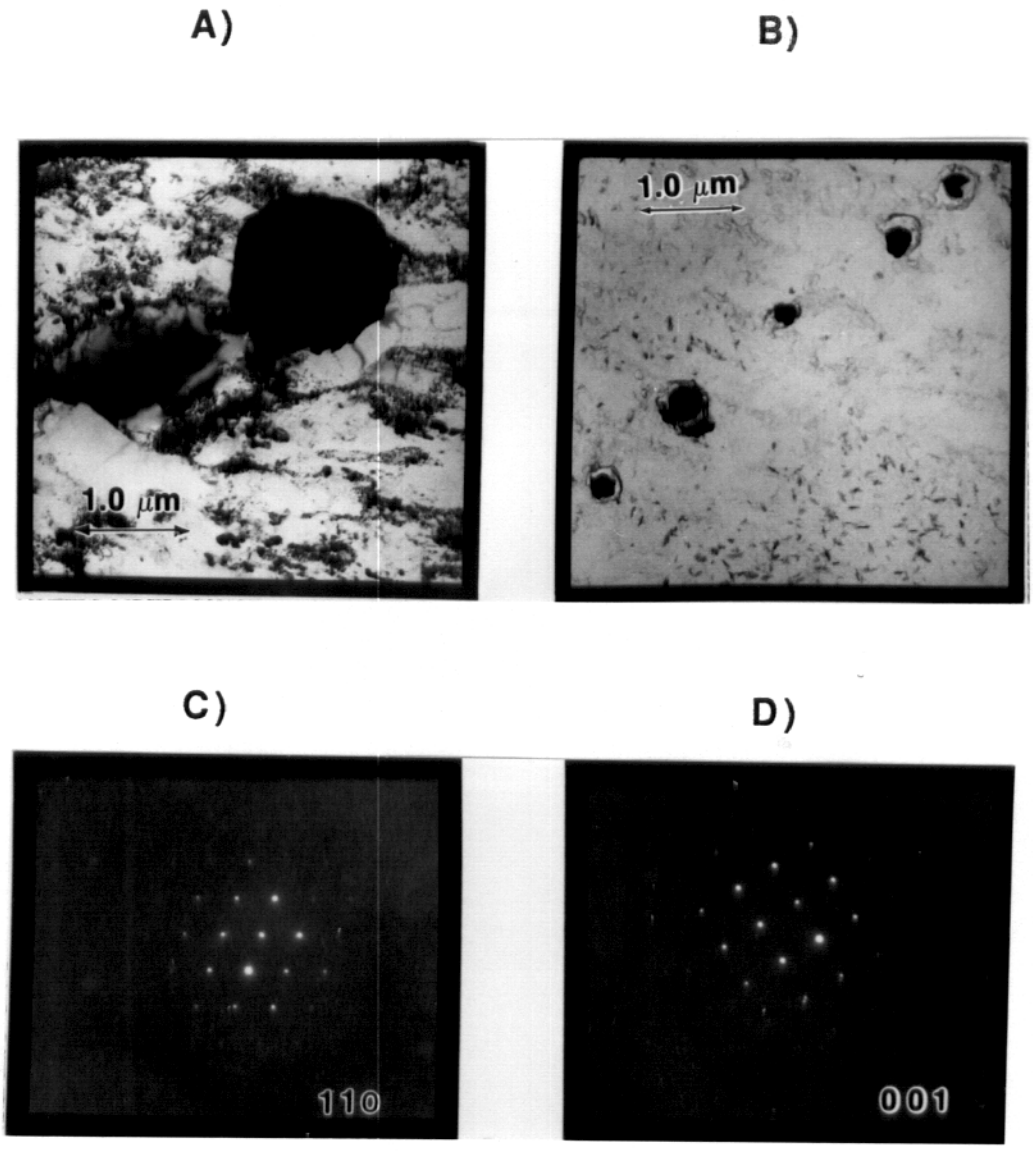

Figure 5.7. a and b) TEM images of MnS. c and d) Microdiffraction patterns from MnS.

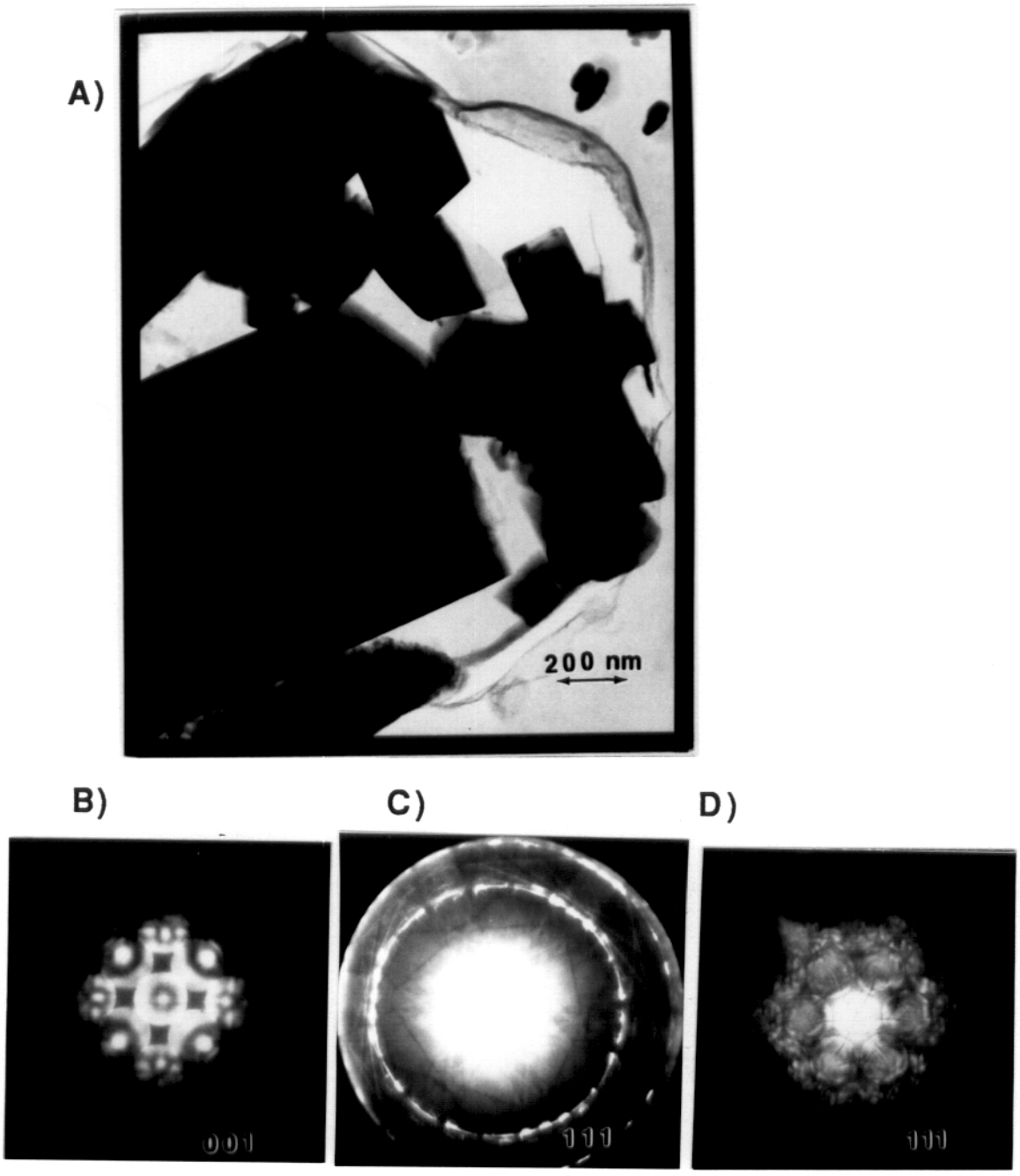

Figure 5.8. a) TEM image of spinel in tempered L9. b, c and d) Convergent beam diffraction patterns from spinel.

compositional analysis. Figure 5.8b,c, and d are two characteristic convergent beam electron diffraction patterns from spinel.

The TEM thin foil images of the tempered and untempered steel are shown in Figure 5.9. The untempered steel consisted of lath martensite with a very high dislocation density which was distributed throughout the laths (Figure 5.9a). No precipitates were present. Tempering between 400°C and 700°C caused the dislocation structure to begin to recover and rearrange itself so that some areas within the laths were relatively dislocation free (Figure 5.9b-g). At 800°C and 900°C, there were areas where the dislocation density became higher and more uniform indicating that new untempered martensite had formed (Figures 5.9h-i).

Aging Results

Optical metallography showed that aging at 520°C and 600°C led to lath coarsening after 1000, 5000 (Figure 5.10) and 10,000 hours (Figure 5.11). Aging at 365°C and 420°C did not change the appearance of the alloy at the optical level. The Vickers microhardness results reflected these results (Figure 5.12). At 365°C and 520°C, the hardness was the same as the steel tempered at 700°C for twenty-four hours. However at 520°C and 600°C the hardness dropped off. The sample which was aged for 5000 hours at 600°C contained delta ferrite (Figure 5.13), which caused the hardness to drop

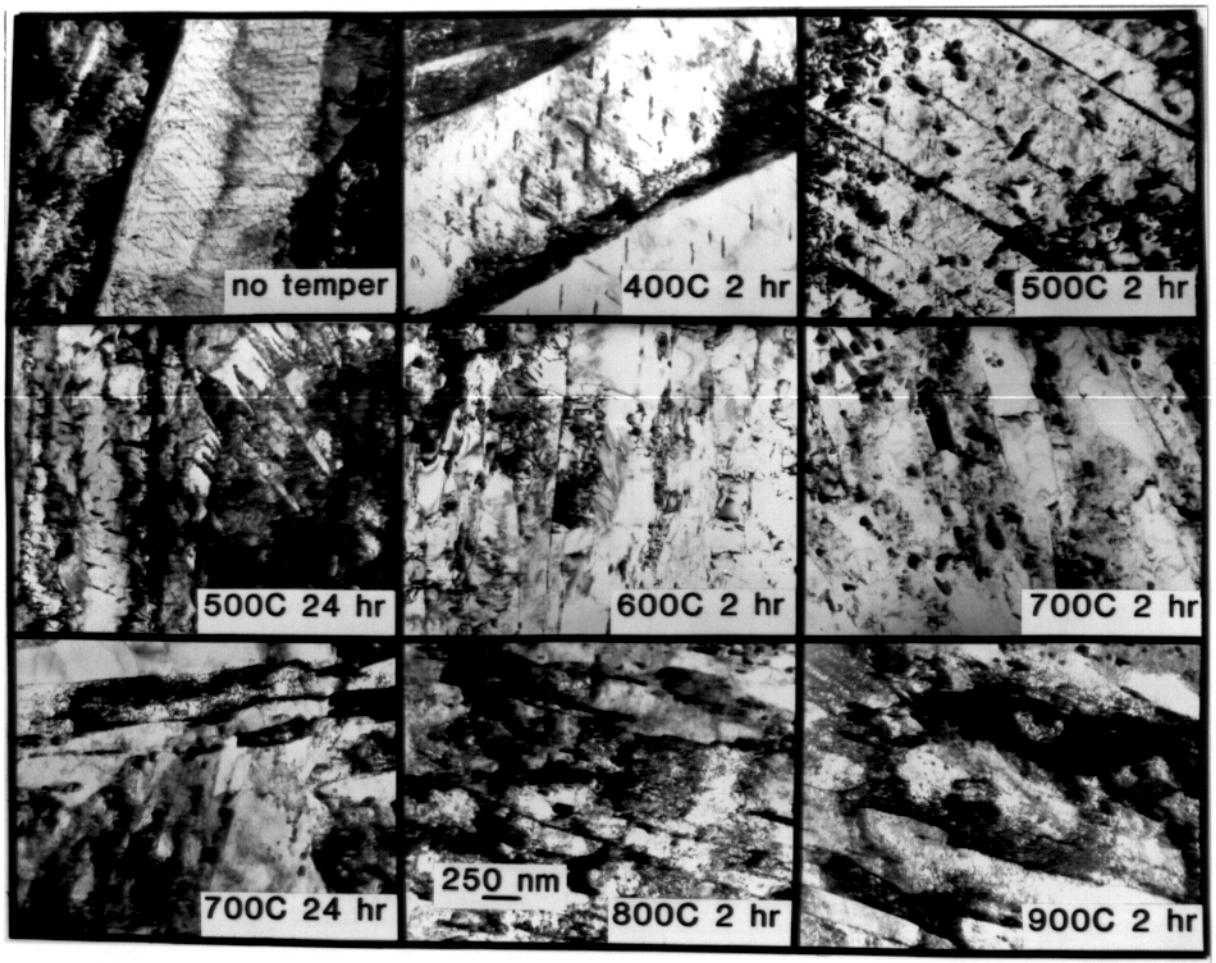

Figure 5.9. TEM images from normalized and normalized + tempered L9.

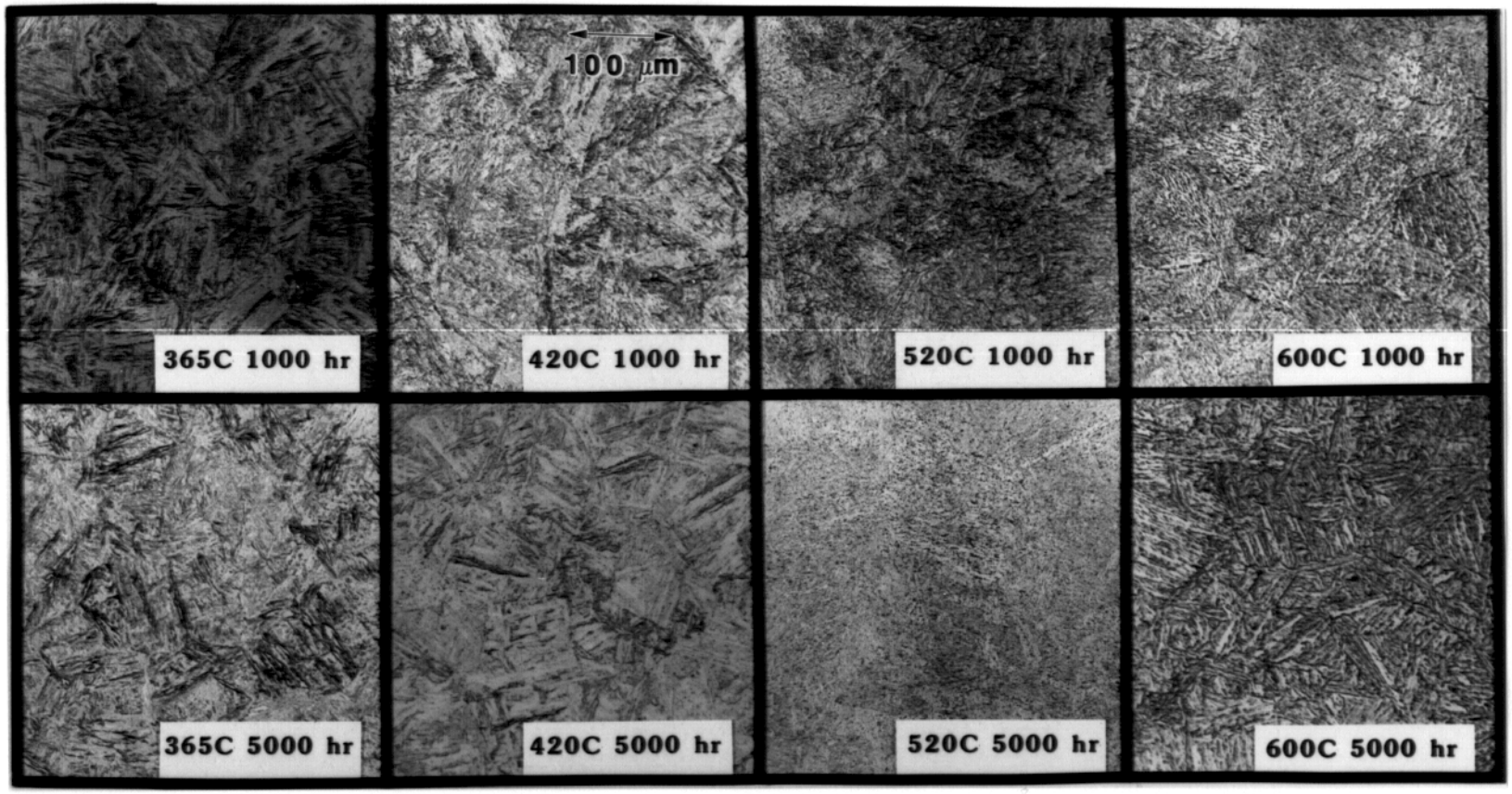

Figure 5.10. Optical micrographs from L9 aged for 1000 and 5000 hours.

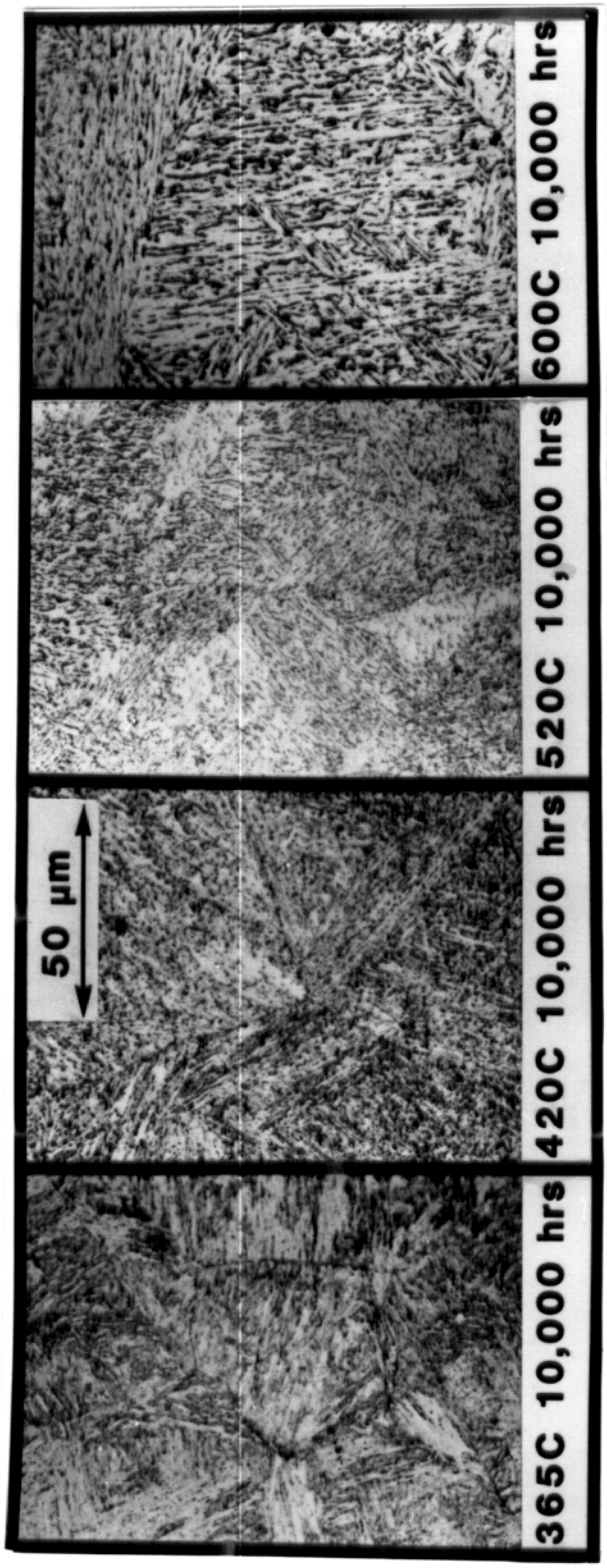

Figure 5.11. Optical micrographs from L9 aged for 10,000 hours.

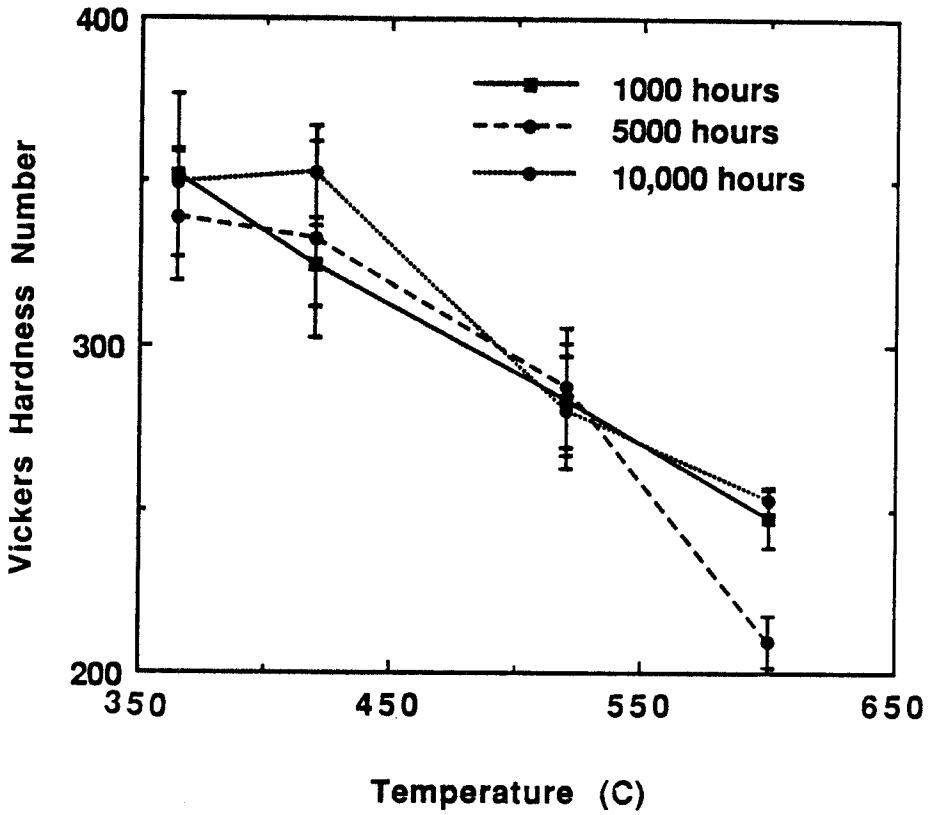

Figure 5.12. Microhardness results from aged L9.

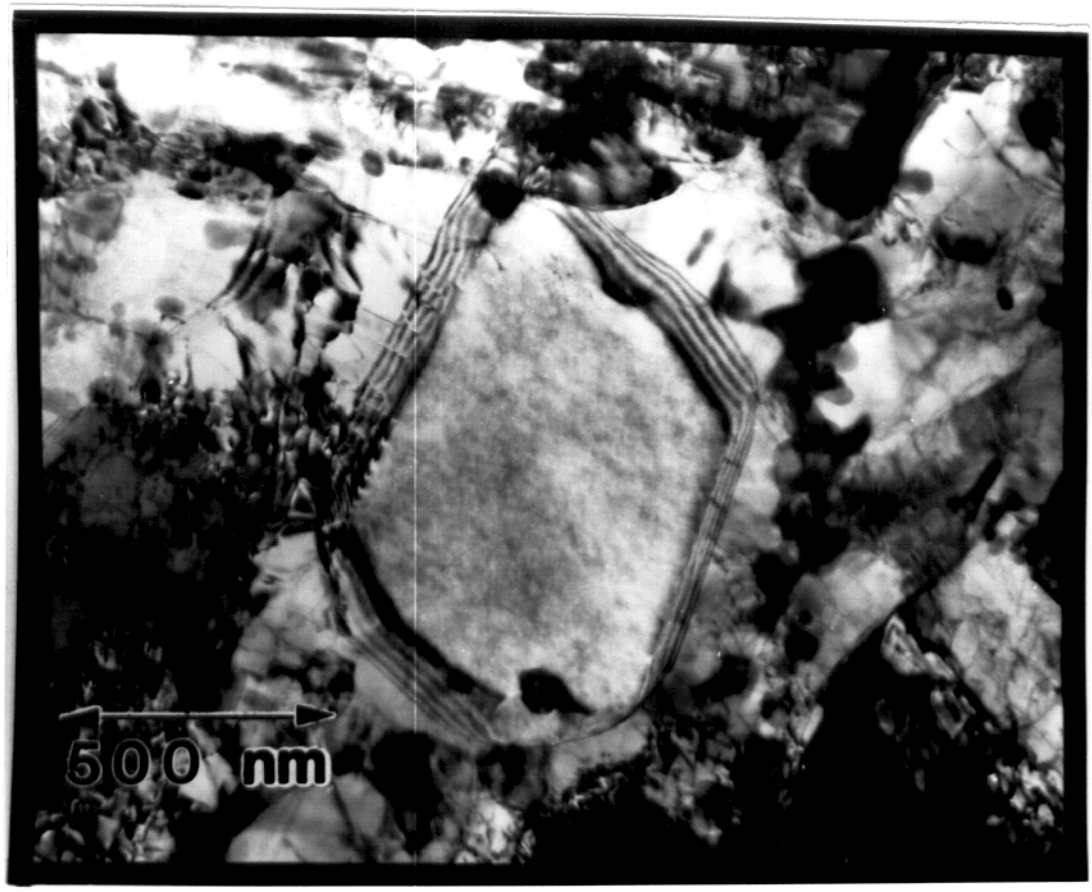

Figure 5.13. Delta Ferrite in L9 aged for 5000 hours at 600°C.

below that of the other samples aged at 600°C. The TEM results reflected these same changes. For example, the sample aged for 10,000 hours at 365°C had an average lath width of 0.5 μm, while that aged for 10,000 hours at 600°C had an average width of 0.3 μm. The $M_{23}C_6$ coarsened from an average size of 60 nm to 100 nm. The higher temperature aging also showed a decrease in dislocation density and the lath boundaries sometimes showed sets of regular dislocations lined up along them. The higher magnification TEM images of the aged samples are shown for the 1000 hour (Figure 5.14), 5000 hour (Figure 5.15), and 10,000 hour (Figure 5.16) samples. The precipitate size also coarsened. In all the aged samples, $M_{23}C_6$ was the only precipitate seen except for one or two VC precipitates. However in the sample aged for 1000 hours at 520°C two isolated examples of chi phase, an intermetallic, were seen. Using EDS the composition of the phase was calculated to be 18% Cr, 16%Mn, 58%Fe, and 8%W (wt%). The selected area diffraction results showed that the chi had a cube-on-cube orientation relationship with the ferrite (Figure 5.17). After aging for 5000 hours, chi phase was found at both 420°C and 520°C, and the amount had increased. After 10,000 hours, chi was uniformly distributed throughout the structure at 420°C and 520°C. The size had increased, particularly at 520°C. Figure 5.18 shows one of these large chi grains in the sample aged for 10,000 hours at 520°C. Order/disorder domains were often present in the larger chi grains, and they sometimes contained $M_{23}C_6$ precipitates. No chi was found in any of the samples aged for 365°C and 600°C.

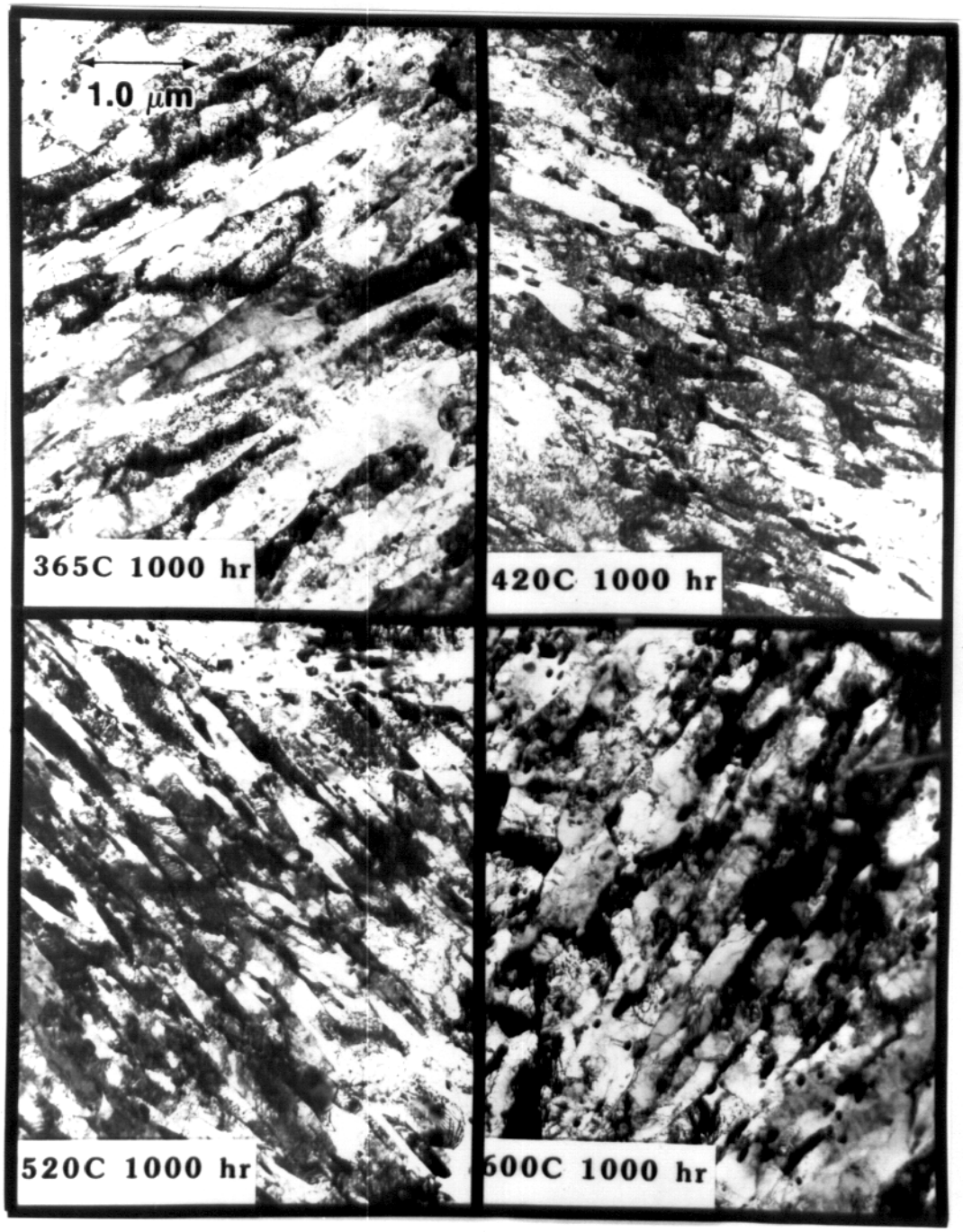

Figure 5.14. TEM micrographs from L9 aged for 1000 hours.

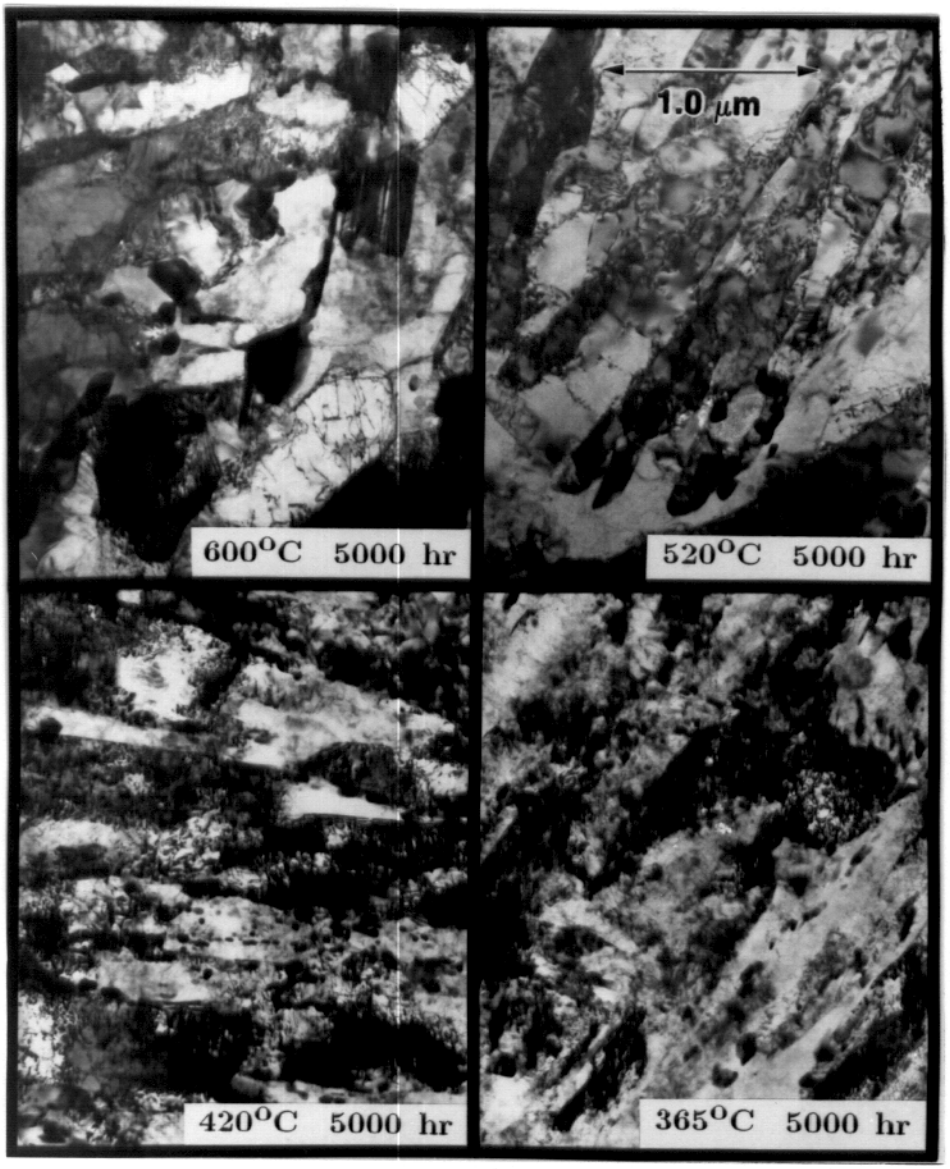

Figure 5.15. TEM micrographs from L9 aged for 5000 hours.

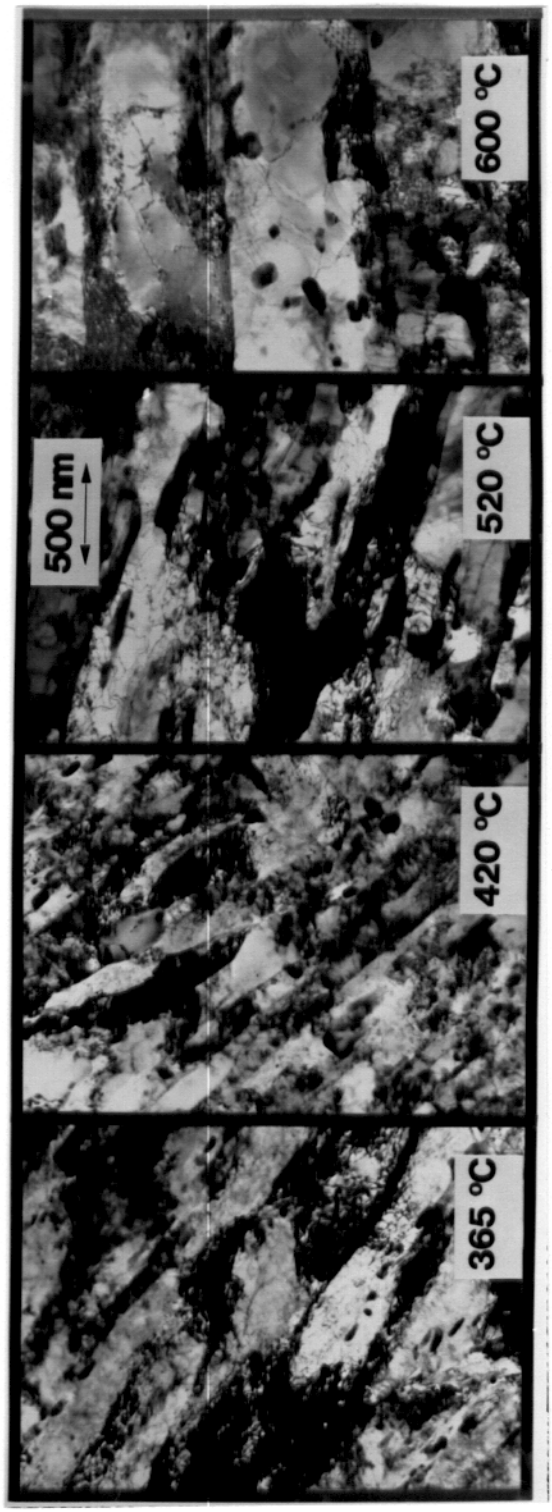

Figure 5.16. TEM micrographs from L9 aged for 10,000 hours.

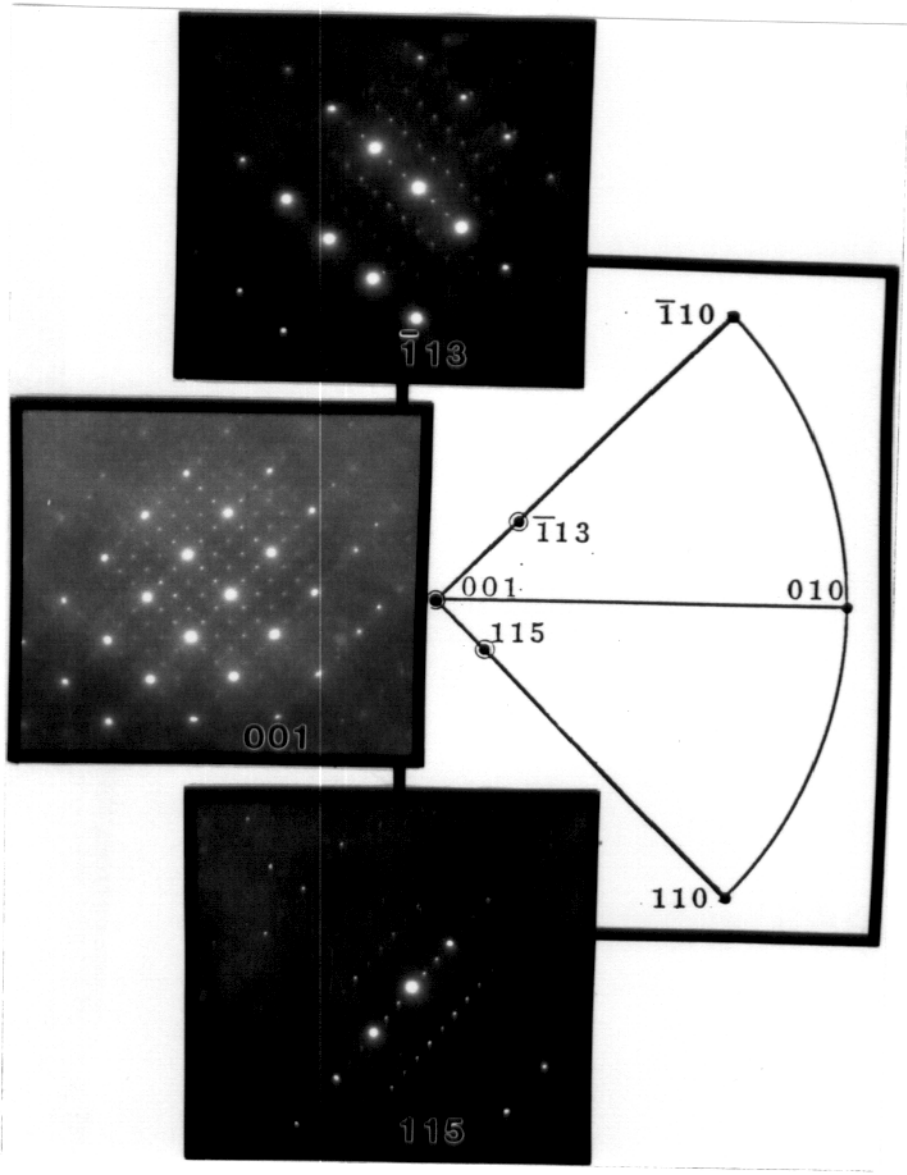

Figure 5.17. SAD tilt sequence showing the orientation relationship between chi and ferrite found in L9.

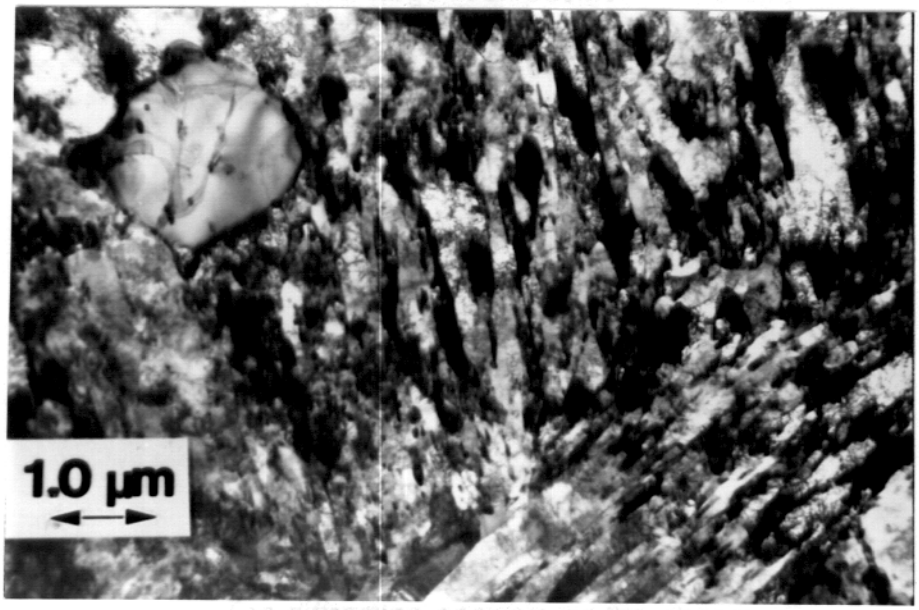

Figure 5.18. Large chi grain in L9 aged for 10,000 hours at 520°C.

Fe-Cr-Mn Ternary Aging Results

Energy dispersive x-ray analysis (EDS) of the samples showed the overall sample composition to be 25 wt% Cr, 12%Mn, and 63% Fe, which deviated slightly from the target composition. The structure of the sample which was rolled only, and those which were aged for 2000 hours were all similar (Figure 5.19) They showed large ferrite grains (approximately 100 μm) with smaller particles within them. TEM analysis of the samples showed the ferrite grains had a very high dislocation density, which can be attributed to the final cold rolling. The particles were shown to consist of a matrix phase with ribbons of a second phase running through it. The structure of these samples is shown in Figure 5.20, where one of the two-phase clumps is surrounded by the ferrite with a high dislocation density. A higher magnification image of the ribbons and matrix surrounding them are shown in Figure 5.21a. The diffraction analysis on the phases (Figures 5.21b and c) showed that the particle matrix was austenite, while the ribbons were $M_{23}C_6$. They had a cube-on-cube orientation relationship.

The sample which was aged for 5000 hours at 520°C showed a marked change from the 2000 hour samples. In this sample, the large ferrite grains with the high dislocation density were replaced with a finer grained structure (approximately 400 nm). The microstructure was a mixture of sigma, ferrite and some austenite. Figure 5.22 shows a TEM image of the microstructure. The large grain in the center is a sigma grain. Figure 5.23 shows a set of

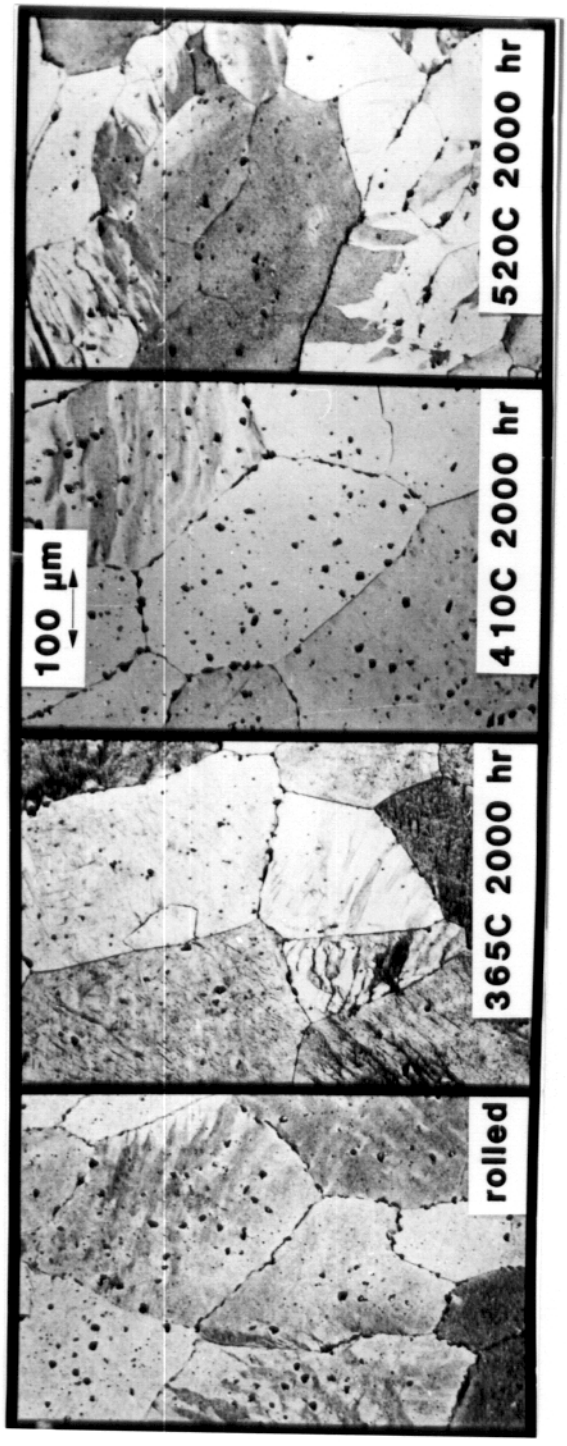

Figure 5.19. Optical micrographs from the Fe-Cr-Mn ternary which was aged for 2000 hours.

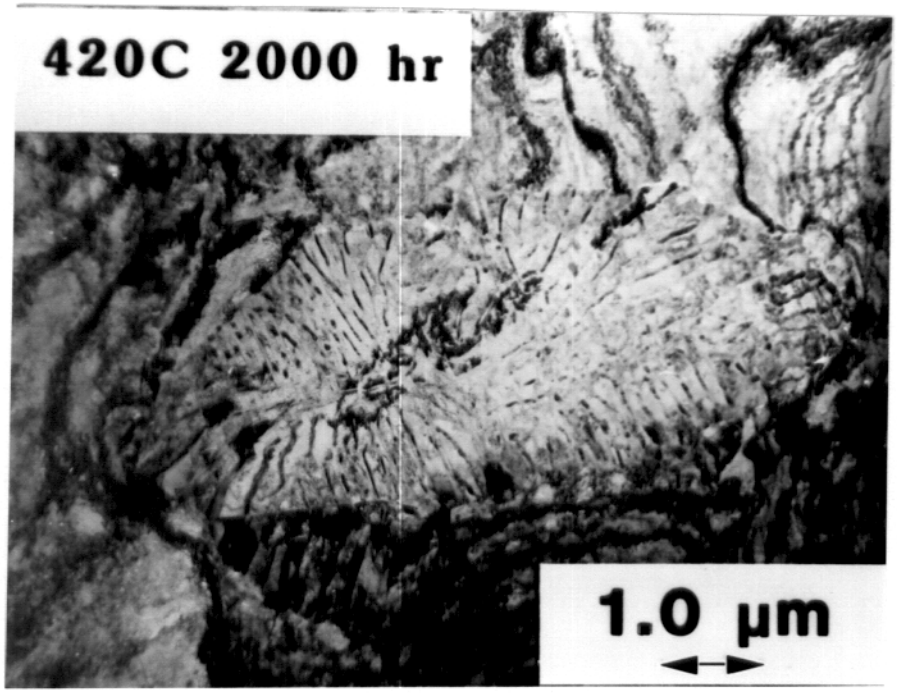

Figure 5.20. Two phase particle sitting in a matrix of ferrite.

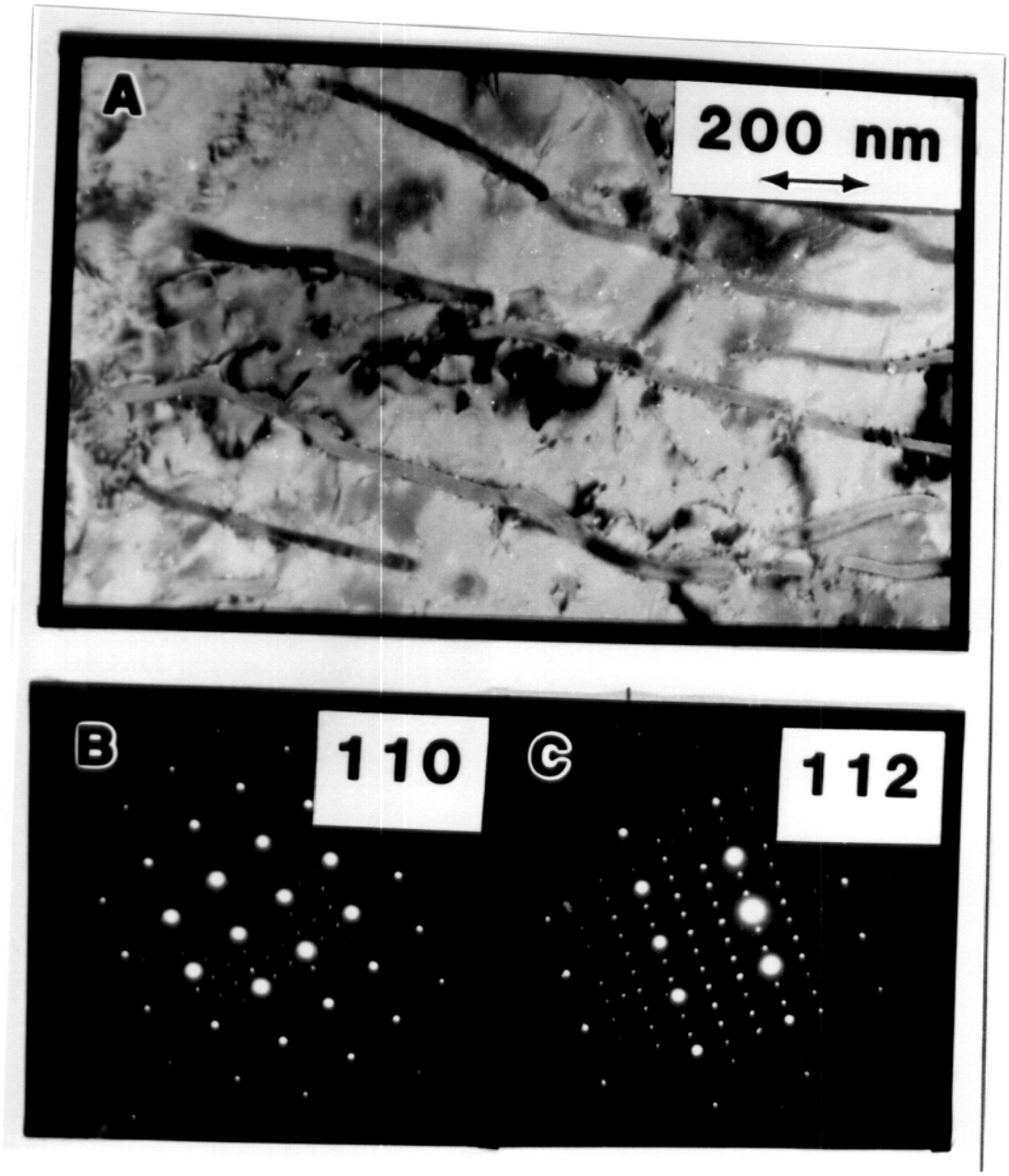

Figure 5.21. a) TEM image showing $M_{23}C_6$ ribbons in an austenite matrix. b and c) SAD patterns showing the cube-on-cube orientation relationship between the austenite and $M_{23}C_6$.

Figure 5.22. TEM micrograph showing the structure of the Fe-Cr-Mn alloy after aging for 5000 hours at 520°C.

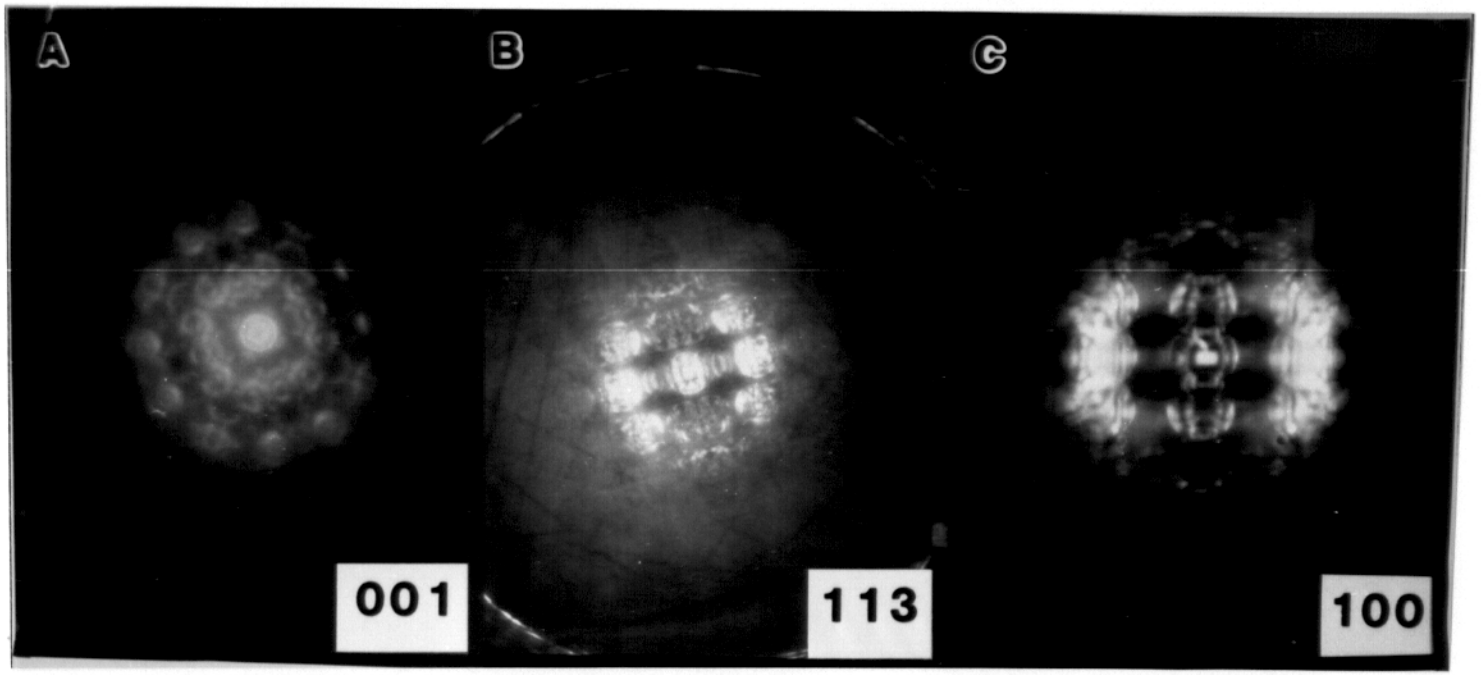

Figure 5.23. Convergent beam diffraction patterns from sigma phase in the Fe-Cr-Mn ternary which was aged for 5000 hours at 520C.

convergent beam diffraction patterns which were used to identify the sigma. No chi was found in the sample.

Chapter 5 Discussion

The tempering study indicated that the A_{c1} temperature for the steel lies in the temperature range between 700°C and 800°C. The observed hardness increase of the specimens tempered at temperatures above 700°C resulted from the austenite transforming to new untempered martensite. There was no indication that the tempered samples had formed new austenite at 700°C. The hardness of the steel dropped off sharply when tempered between 500°C and 700°C because of the decrease in the dislocation density and the change in the precipitates from M_3C to $M_{23}C_6$. In a few of the aged samples, localized areas where austenite was present were seen. But this was probably due to local composition inhomogeneities in the steel as they were not found to be related to the temperature or time of aging.

Samples which were aged at 365°C and 420°C for 1000, 5000, and 10,000 hours maintained a hardness close to that of the samples tempered at 700°C. However, as the aging temperature increased, the hardness dropped off continuously in consequence of the recovery of the dislocation structure and the coarsening of the precipitates and laths. It is interesting to compare this hardness drop with that of several other 11-13%Cr, martensitic steels (2). Table 5.1 shows the composition and heat treatment prior to aging for

9000 hours at 600°C. Aging of FV448 for 9000 hours caused a 14% reduction in the Vickers hardness number. Aging of CRM 12 for 9000 hours led to a 6% reduction in hardness, and aging FI for 9000 hours at 600°C led to a 12% reduction in the hardness. But the hardness of L9 dropped 28%

Table 5.1 Composition (wt%) and Normalizing and Tempering Treatments of 11-13% Cr, Martensitic Steels

Steel	Cr	C	Mn	Ni	Mo	V	Nb	Heat Treatment
CRM12	12	0.2	0.5	0.6	0.96	0.3	----	1050°C/2hr, 760°C/2.5hr
FV448	11	0.1	0.9	0.6	0.6	0.14	0.26	1020°C/1hr, 700°C/1hr
FI	13	0.05	0.5	0.4	----	----	----	1000°C/1hr, 750°C/2hr

when it was aged for 10,000 hours at 600°C. This is probably because the addition of Mn decreased the A_{c1} so that when the sample is aged at 600°C, the higher Mn steel recovered more. But, it should also be noted that the starting hardness of L9 was higher than that of all three of the steels, so the final hardness is only lower than that of FV448. However, this difference may be due to normalizing and tempering differences.

As can be seen by comparing the hardness of the samples aged for different times at 600°C, the changes which occurred in this steel occurred before 1000 hours. This stability can be attributed to the stability of the $M_{23}C_6$. Although the $M_{23}C_6$ coarsened with an increased aging

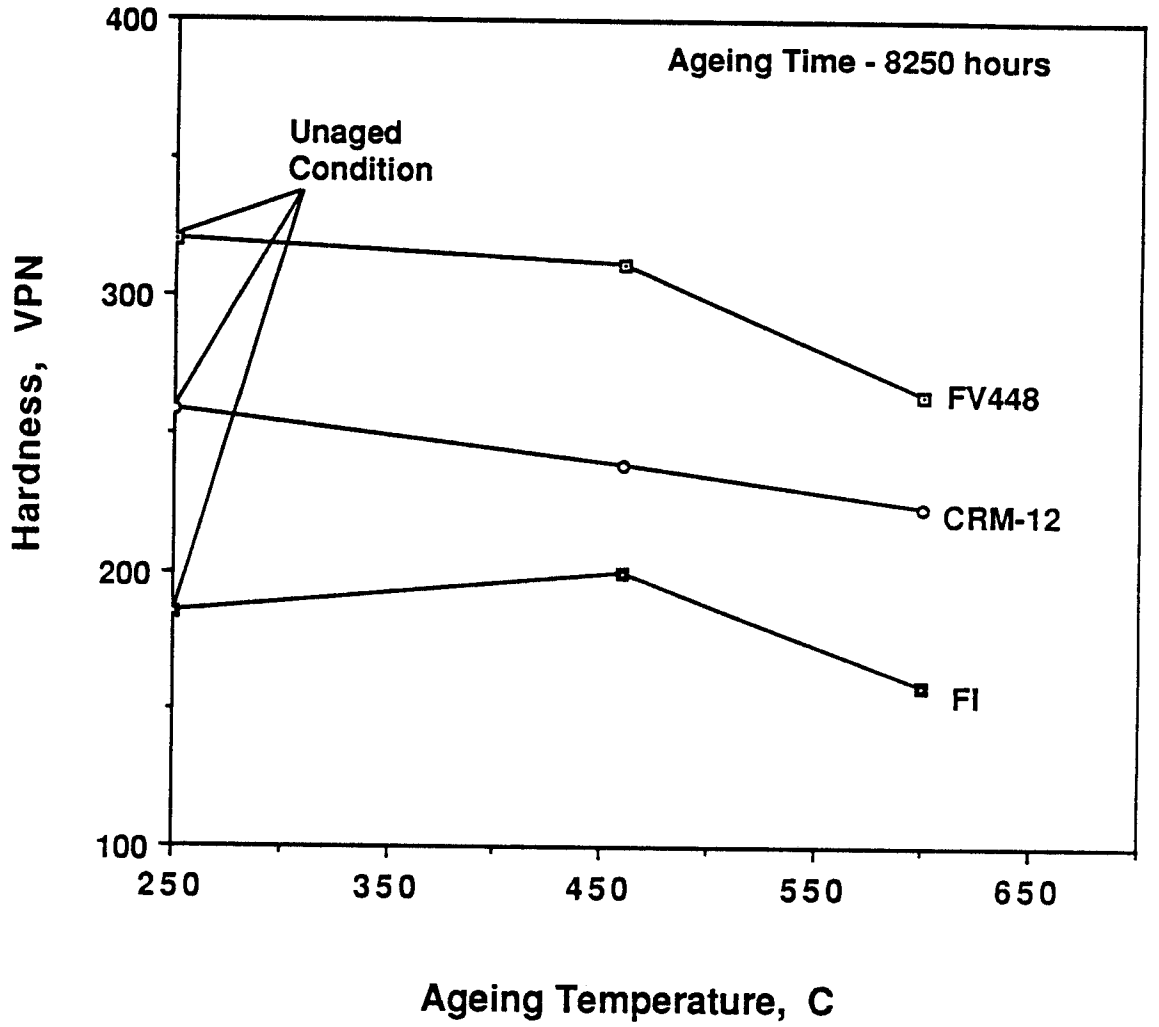

Figure 5.24. Vickers Hardness number versus aging temperature for the aged 11-13% Cr, martensitic steels.

temperature, it was still somewhat effective in preventing recovery of the martensitic structure.

$M_{23}C_6$ was the equilibrium carbide which formed in the steel during the heat treatments. Two hour tempers at 400°C and 500°C hours led to the formation of M_3C within the martensite laths, but this phase is probably metastable because tempering at 500°C for twenty-four hours led to $M_{23}C_6$ formation in addition to the M_3C and $M_{23}C_6$. Also, aging at 365°C and 420°C, did not lead to the formation of M_3C.

The chi phase was found in the steel after aging at 420°C and 520°C, with the amount increased with a longer aging time. No chi was found at 365°C or 600°C, and was not seen in the sample when it was tempered for two and twenty-four hours. This indicates that in this steel, it's formation is very sluggish, and that it only forms at temperatures less than 600°C. At 365°C, the aging time was not long enough to nucleate chi phase.

Although chi phase is often thought of as an Fe-Cr-Mo intermetallic, there is also an Fe-Cr-W chi. The formation of chi phase was first discovered in 1949, in an alloy steel (3). It was postulated that chi was associated with Mo and possibly W. In a more detailed work (4), 3.0% Mo was set as the lower limit for chi formation in austenitic stainless steels. Koh (5) found chi in a steel with 1.62% Mo and 0.91% W and from this concluded that Mo and W act similarly in promoting chi. Chi phase was also found in an 40% Fe, 20 % Cr, 40% W alloy (6). Goldschmidt did work on the Fe-Cr-W system and found an Fe- Cr-W chi which was an equilibrium phase in the system (7). So there is ample evidence that chi forms in Fe-Cr-W alloys.

The formation of large amounts of chi phase in heat treated steels at levels of Mo and/or W where at the most only very small amounts of chi would be expected has been documented in two Chinese papers. In an austenitic steel with 0.4C, 31Mn, 3.0Al, 2.5Cr, 1.5Mo, 0.5W, 0.2Nb, 0.01B, 1.5V, chi formed at 650°C after aging between 520 and 5000 hours. It was concluded that chi formation was accelerated by Cr (8). In a steel with 0.70C, 17Cr, 14Mn, 2Mo, .3N, .3Si, chi formed at 550°C, 650°C, 750°C, 850°C, 900°C, 950°C in times as short as five minutes (9). It was concluded that both Mn and Cr accelerate chi phase formation. In 12% Cr, 0.1C martensitic steels (with <2%Mn), intermetallic formation is not expected until Mo levels reach 3%. It was also reported that intermetallics were less likely to form with W than with Mo (10), and yet in the 12Cr-6.5Mn-0.1C-1W-0.3V steel, aging from 1000 -10,000 hours at 420°C and 520°C led to the formation of chi. After 10,000 hours at 420°C and 520°C, the presence of chi was common. The Fe-Cr-Mn austenitics have also shown a tendency to be unstable. Both sigma and ε-martensite can form so that careful alloying is needed to ensure a stable microstructure (11). This study has shown a similar problem in a martensitic Fe-Cr-Mn steel. But while sigma and ε-martensite are expected phases in the Fe-Cr-Mn system, there is no chi phase in the published Fe-Cr-Mn phase diagrams at these compositions (12).

The Fe-Cr-Mn samples were made with a composition close to that of the chi phase which formed in L9. They were then aged at the temperatures and times at which chi formed in L9. But investigation of the material did not show the formation of any chi phase. The presence of $M_{23}C_6$ indicated that

there was carbon present in the alloy. It has been suggested that carbon is needed for chi phase formation (13), but although it was present in this alloy, chi still did not form. Only the phases expected in the Fe-Cr-Mn-C system were found (12). It is interesting to note that the sample maintained it's cold-worked structure for quite a long time (between 2000 and 5000 hours). The formation of chi in L9 was also quite sluggish, leading to the suggestion that these Fe-Cr-Mn alloys do not transform quickly. The only evidence found for chi phase formation in simple Fe-Cr-Mn alloys where Mo and W are not present was in Fe-Cr-Mn austenitic ternaries which were irradiated in FFTF at 420°C (14). In these alloys, chi formed inside bcc grains which had formed during the irradiation and at austenite grain boundaries (15). No report of chi phase formation was found in any unirradiated Fe-Cr-Mn steels which did not contain W or Mo.

References for Chapter 5

1. Der Hing Huang and G. Thomas *Met. Trans.* 2 (1971) 1587.

2. E.A. Little and L.P. Stoter, in *Effects of Radiation on Materials: Eleventh Conference ASTM STP 782* , H.R. Brager and J.S. Perrin, Eds., ASTM (1982) pp. 207-233.

3. K. W. Andrews *Nature* No. 4180 (1949) 1015.

4. K.W. Andrews and P.E. Brookes Metal Treatment and Drop Forging July 1951 p. 301.

5. P.K. Koh, *Trans AIME* 197 (1953) 339.

6. K. Kuo discussion of F.L. Ver Snyder and J.H. Beattie Jr. *Trans ASM* 47 (1955) 211.

7. H.J. Goldschmidt *High-temperature Steels and Alloys for Gas Turbines* , The Iron and Steel Institute, London, (1952) 249.

8. Y. Zheng, F. Zhang, H. Gao, G. Wang, *Acta Metallurgica Sinica* 20(1) (1984) A1.

9. S.L. Chen and T.Y. Feng, *Acta Metallurgica Sinica* 14(2) (1978) 152.

10. K.J. Irvine, D.J. Crewe and F.B. Pickering, *JISI* 195(8) (1960) 386.

11. P.J. Maziasz and R.L. Klueh presented at the *14th International Symposium on Effects of Radiation on Materials* Andover MA June 27-29, 1988.

12. E.A. Brandes and K.F. Flint, *Bulletin of Alloy Phase Diagrams* 2(1) (1981) 1037.

13. H.J. Goldschmidt , *Interstitial Alloys* Plenum Press, New York, (1967) 126.

14. J.M. McCarthy and F.A. Garner, *J. Nuc. Mat.* 155-157 (1988) 877.

15. J.M. McCarthy in *Fusion Reactor Materials Semiannual Progress Report for Period Ending March 31, 1989*, DOE/ER-0313/6 p. 103.

Chapter 6: Irradiation Results

Neutron Irradiation Results

The sample irradiated at 600°C to 15 dpa showed a much lower dislocation density, and a coarsening of the $M_{23}C_6$ past what was seen in the samples aged at 600°C. A somewhat more equiaxed ferrite structure developed, but the original lath shape of the grains was still evident (Figure 6.1). The only precipitates found were $M_{23}C_6$. Irradiation led to a mottling of the $M_{23}C_6$ so that they were easily identified. No voids were found in the sample. There was a large fraction of the sample which contained what was identified as austenite grains. In Figure 6.2, a TEM image of an austenite grain containing stacking faults is shown. The EDS spectrum showed that the austenite grains had a higher Mn content than the surrounding ferrite grains. In other areas of the sample, no austenite grains were present.

In the samples which were irradiated at 520°C, large chi grains were found. These tended to form at the lath boundaries (Figure 6.3). As the irradiation dose increased from 14 to 48 dpa, the size of the chi also increased and the ferrite grains became more equiaxed in some areas (Figure 6.4). The amount of chi which formed was much greater than that which formed in the aged samples. The composition of the chi which formed did not appear to be different from that which formed in the aged samples. $M_{23}C_6$ was the only carbide found in these samples. Again, irradiation led to

a much lower dislocation density than that found in the aged samples. No voids were found in either the chi or ferrite grains.

The samples irradiated at 420°C were the only samples which developed voids. Few were seen at 14 dpa, but as the dose increased, more formed. However, even at 114 dpa, their distribution was uneven and their density was very low. A few large dislocation loops were found. The lath shaped structure of the grains was retained in these samples, with some recovery in the 114 dpa sample. $M_{23}C_6$ was the only carbide found in the steel irradiated at 420°C, but irradiation did lead to the formation of small precipitates which were tentatively identified as α'. At 14 dpa, the distribution of α' was uneven. Their size was approximately 50 nm. As the irradiation dose increased, the α' coarsened to 100 nm, but the distribution remained uneven. Figure 6.5 shows a set of TEM images from the samples irradiated at 420°C. A few voids and α' precipitates can be seen.

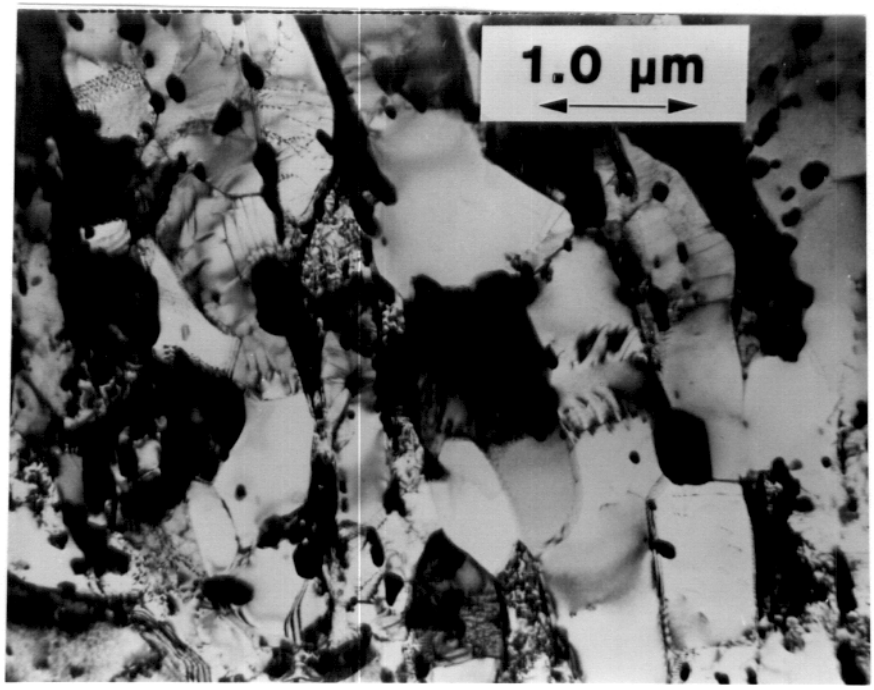

Figure 6.1. TEM micrograph from L9 neutron irradiated at 600C to 14 dpa.

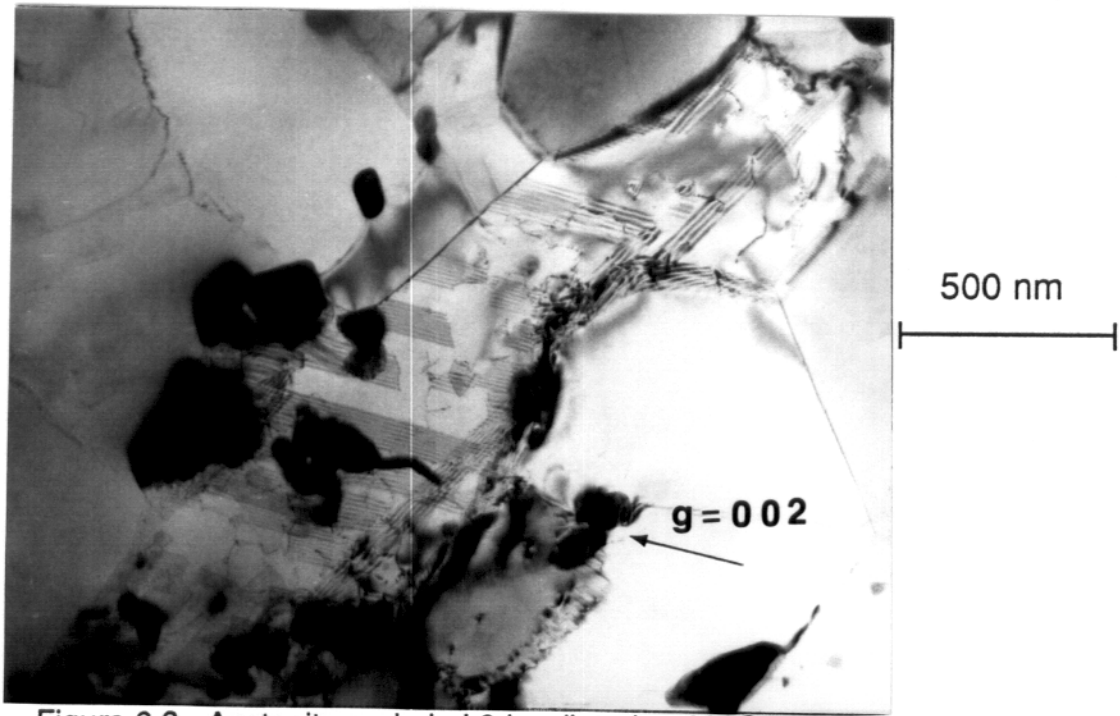

Figure 6.2. Austenite grain in L9 irradiated at 600C to 14 dpa.

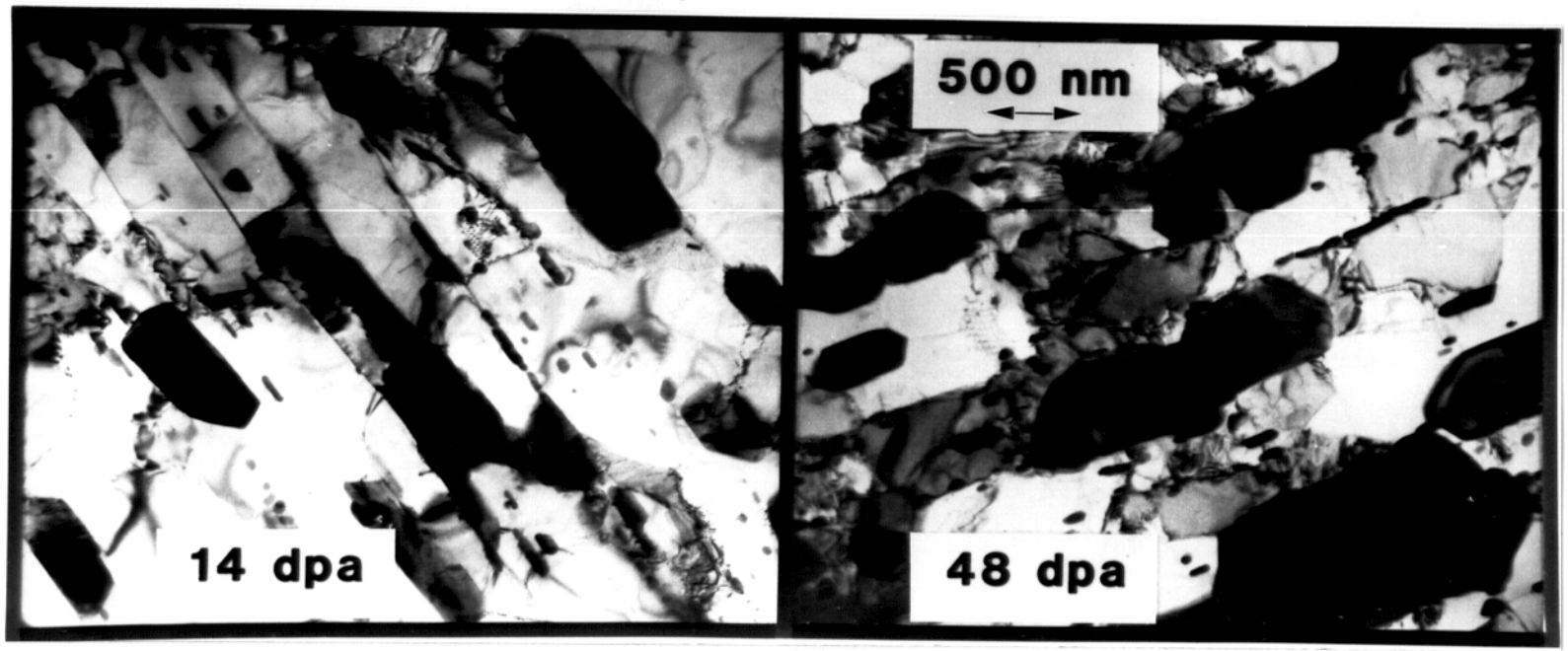

Figure 6.3. L9 irradiated at 520C. Large dark grains at lath boundaries are chi.

Figure 6.4. L9 neutron irradiated to 48 dpa at 520°C. The smooth grains are chi.

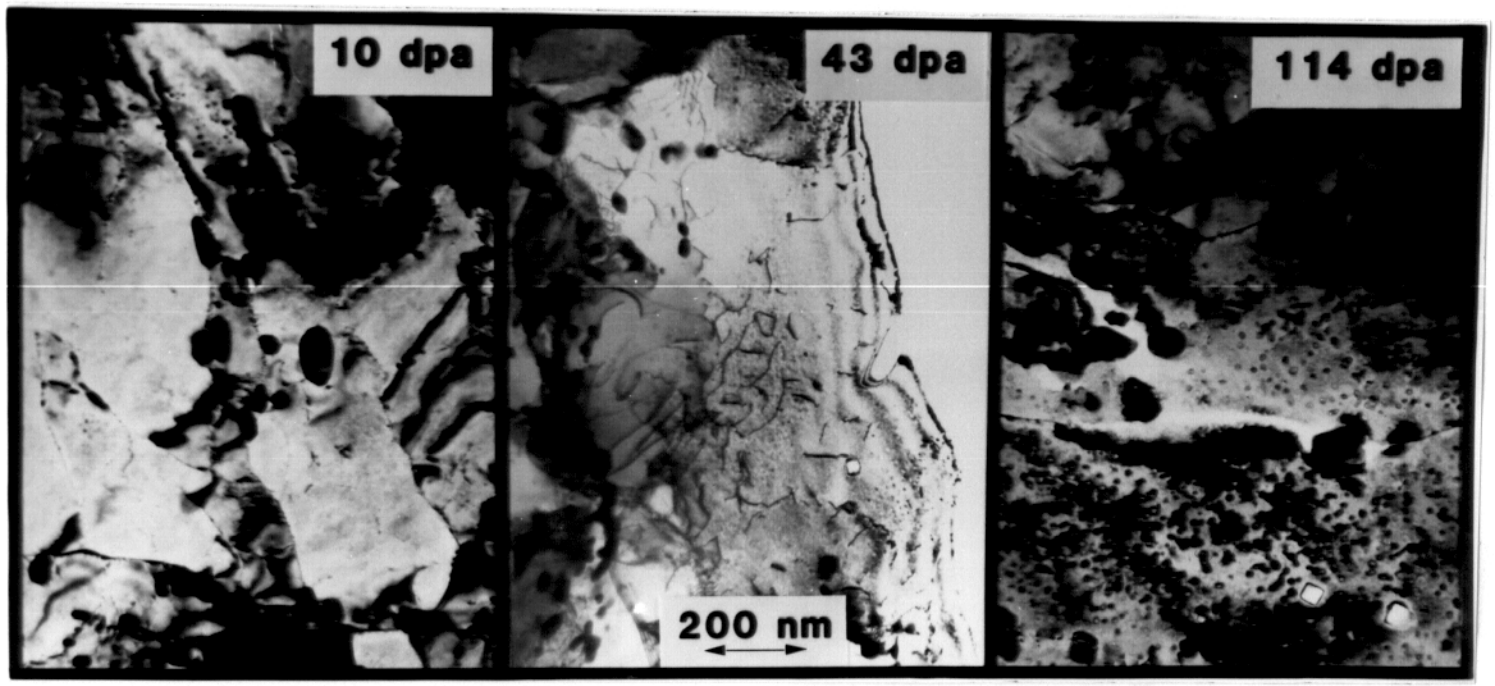

Figure 5.4. L9 neutron irradiated at 420C. Note the alpha prime particles and the voids.

Ion Irradiation Results

Iron irradiations at 450°C, led to the formation of some very small loops (Figure 6.6). As the irradiation dose increased, there were many areas where the dislocations were found to be lined up. At the highest dose, there may have been some transformation to more equiaxed grains. But in most areas, the lath shape of the ferrite grains were still present. The dislocation density present prior to the irradiation remained, and perhaps even increased. Figure 6.7 shows TEM images of L9 irradiated at 450°C. No voids were found in these samples The only precipitate present was $M_{23}C_6$; it's size and distribution were uneven as seen in the unirradiated samples.

Irradiation at 650°C led to a large decrease in the dislocation density, and the lath shaped ferrite grains were often transformed to more equiaxed grains, particularly as the dose increased (Figure 6.8). Almost no dislocation loops were found, with the exception of a few in the highest dose sample. The size of these loops was larger than those found in the samples irradiated at 550°C and 450°C. Irradiation led to a much more uniform size and shape of the $M_{23}C_6$ found in these samples. There may have been a reduction in the amount of $M_{23}C_6$ present, but this is difficult to say as its distribution often varied in the heat treated samples. No other precipitates were found. At this temperature, no voids were seen.

Irradiation at 550°C caused the dislocation density to decrease, but it did not decrease as much as the samples irradiated at 650°C (Figure 6.9). The grains also became somewhat more equiaxed, but again, not as much

as they did at 650°C. Some dislocation loops were seen in the samples irradiated at 550°C (Figure 6.10). There was a mixture of grains with a very low dislocation density, and those with dislocations and loops. The only precipitate seen in these samples was $M_{23}C_6$, the size and shape of which still varied widely. Only two grains containing voids were found in the samples irradiated at 550°C (Figure 6.11). However, at the higher fluences, helium bubbles were often seen. In the 16 dpa sample, the bubble distribution was quite uneven. But at 40 dpa, the bubbles were somewhat more uniformly distributed. The number density was approximately 4 x $10^{13}/cm^2$. Bubbles were seen at lath boundaries, subgrain boundaries and within grains (Figure 6.12). The average size of these bubbles was 3 nm.

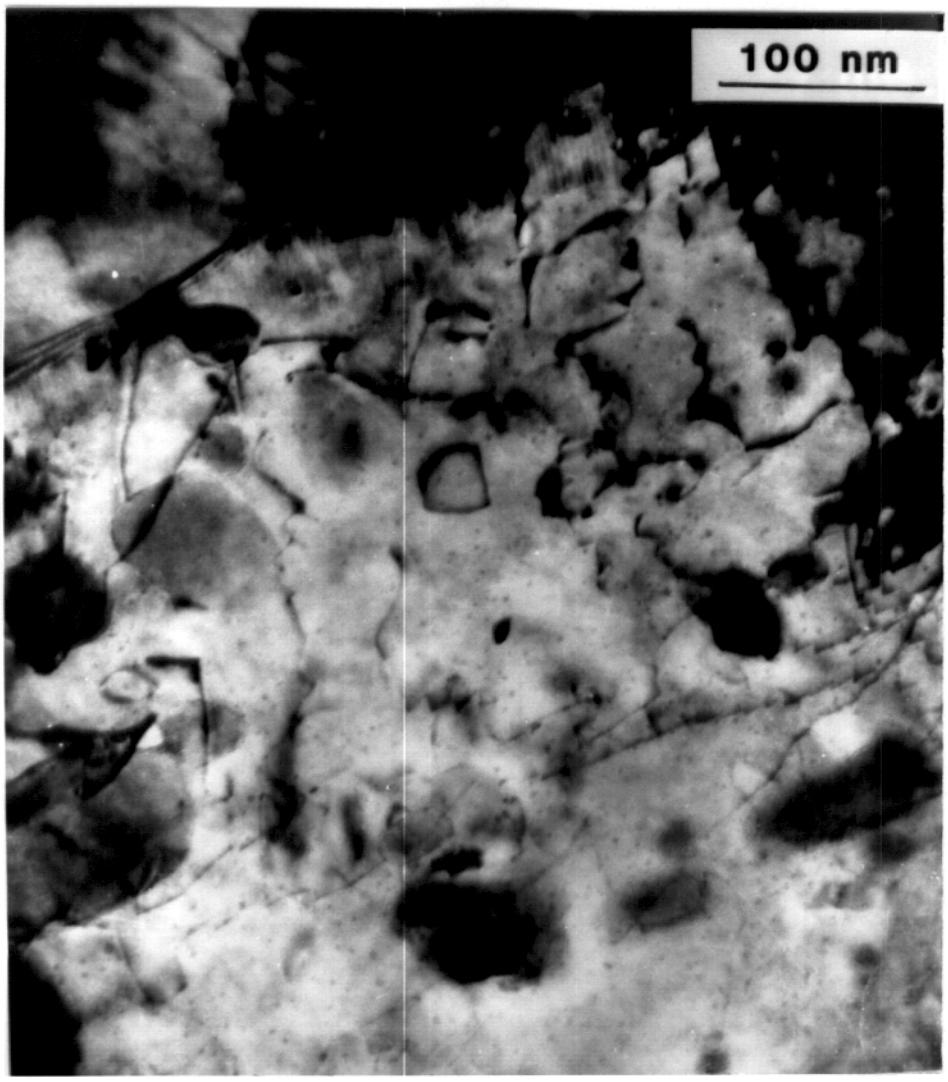

Figure 6.6. Small dislocation loops in L9 which was ion-irradiated at 450°C.

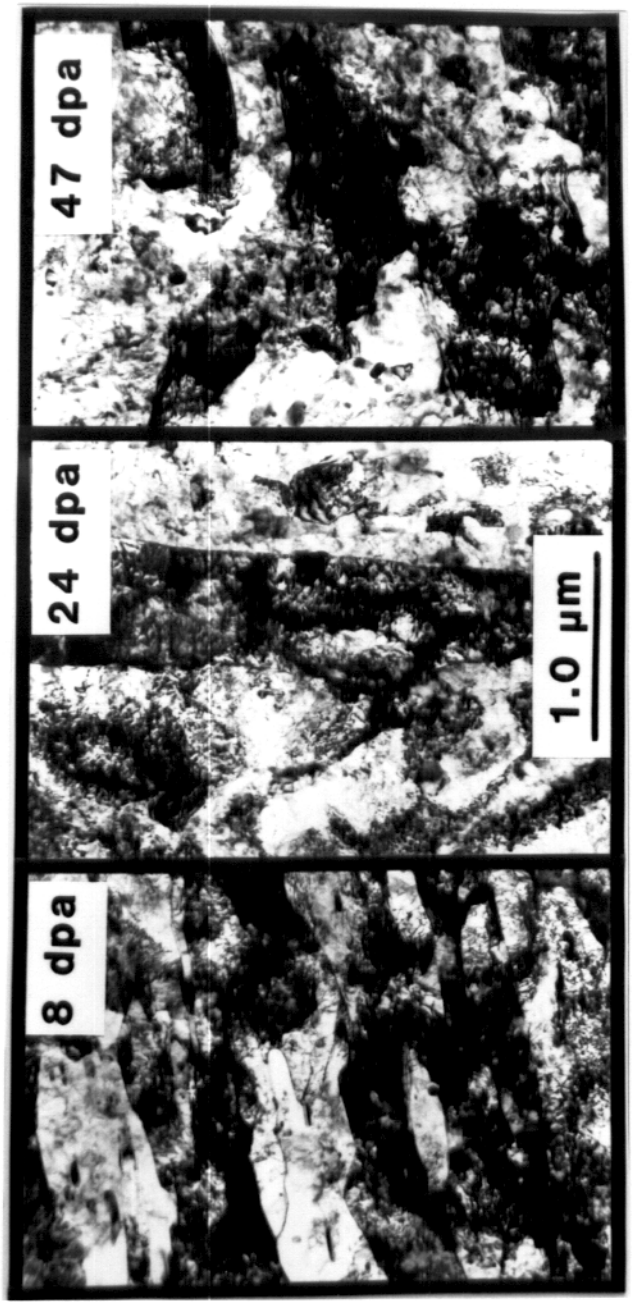

Figure 6.7. TEM micrographs of L9 ion-irradiated at 450C.

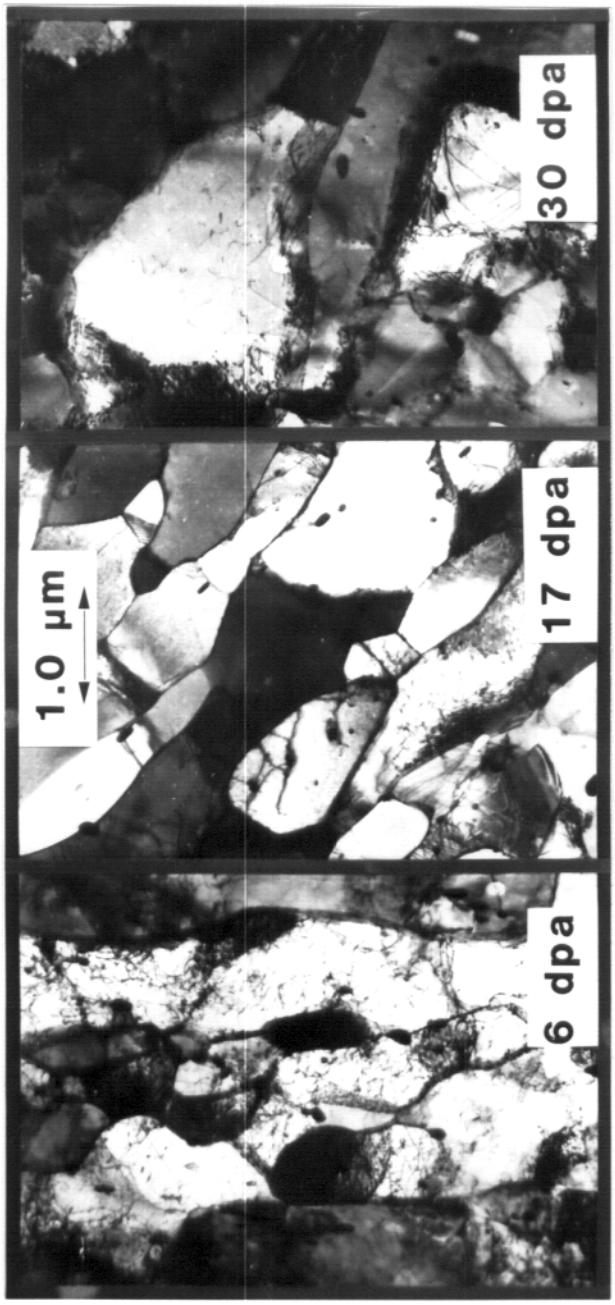

Figure 6.8. TEM micrographs showing the structure of L9 ion-irradiated at 650C.

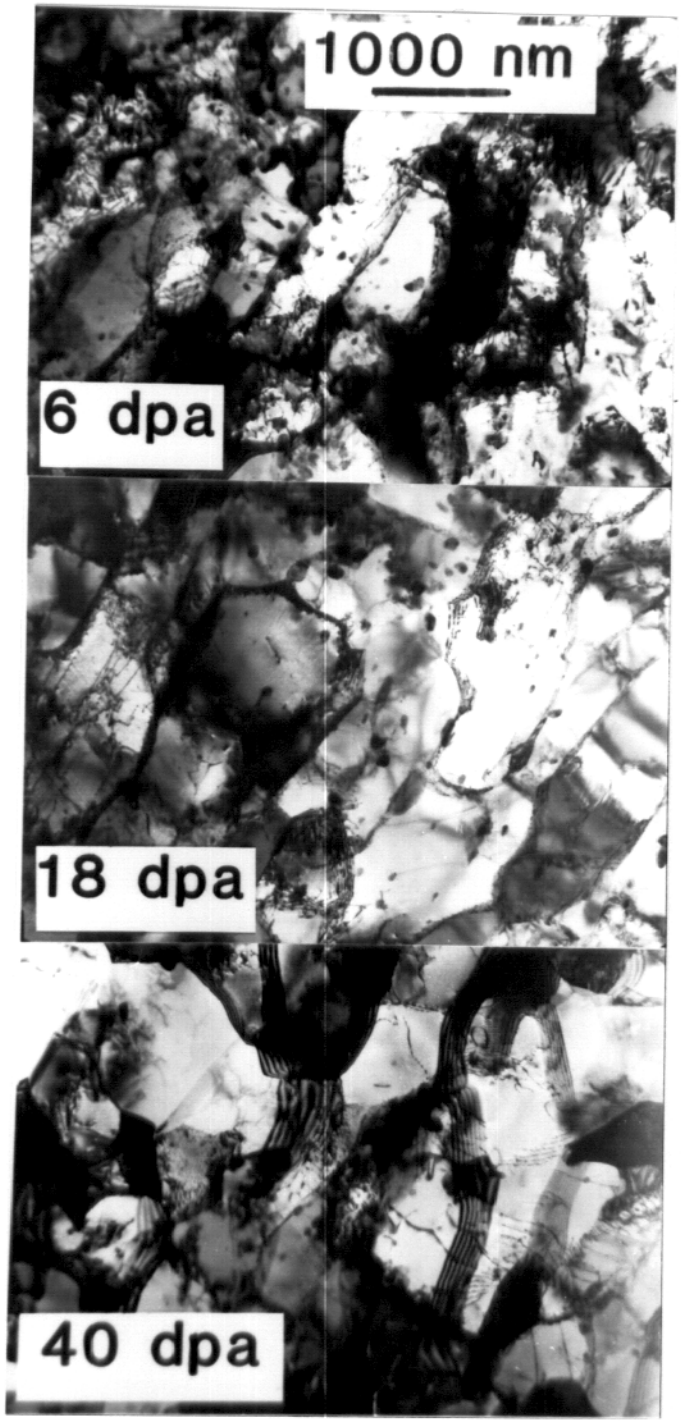

Figure 6.9. TEM micrographs showing the microstructure of L9, ion-irradiated at 550°C.

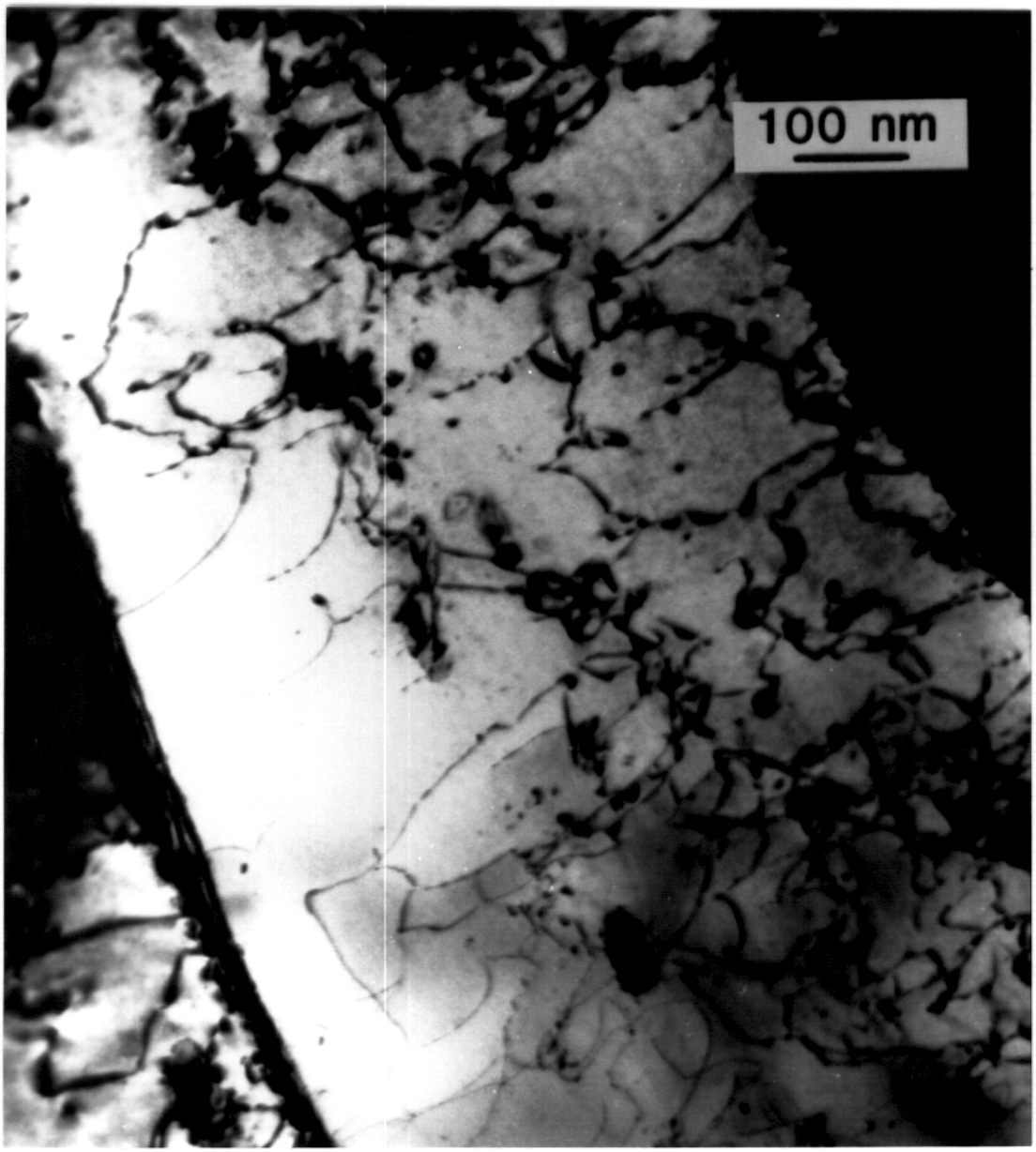

Figure 6.10. TEM micrograph showing dislocation loops in L9 after ion irradiated at 550°C to 40 dpa.

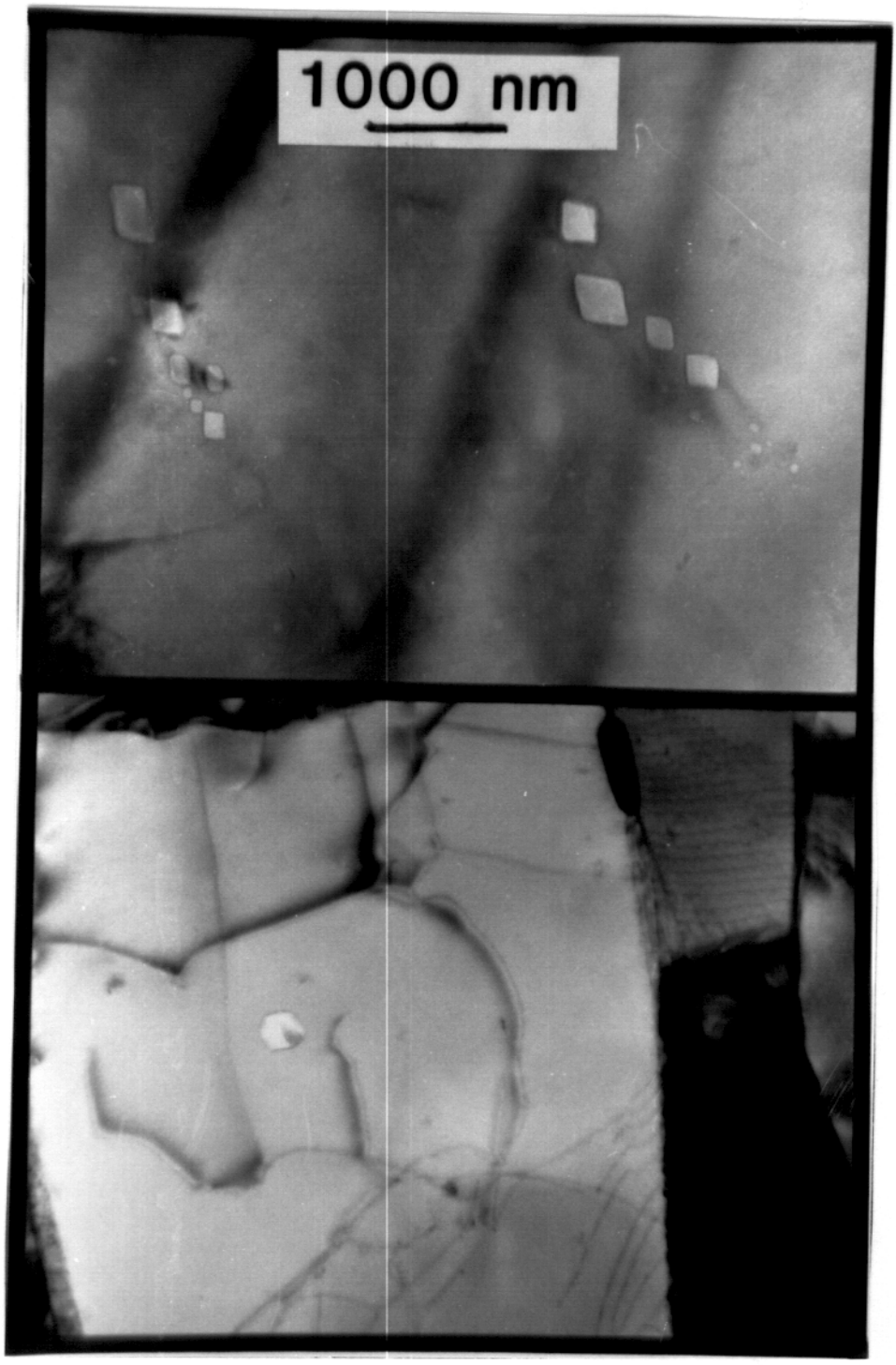

Figure 6.11. TEM micrographs showing the only voids found in L9 after ion irradiation at 550°C (top image 18 dpa, bottom image 40 dpa).

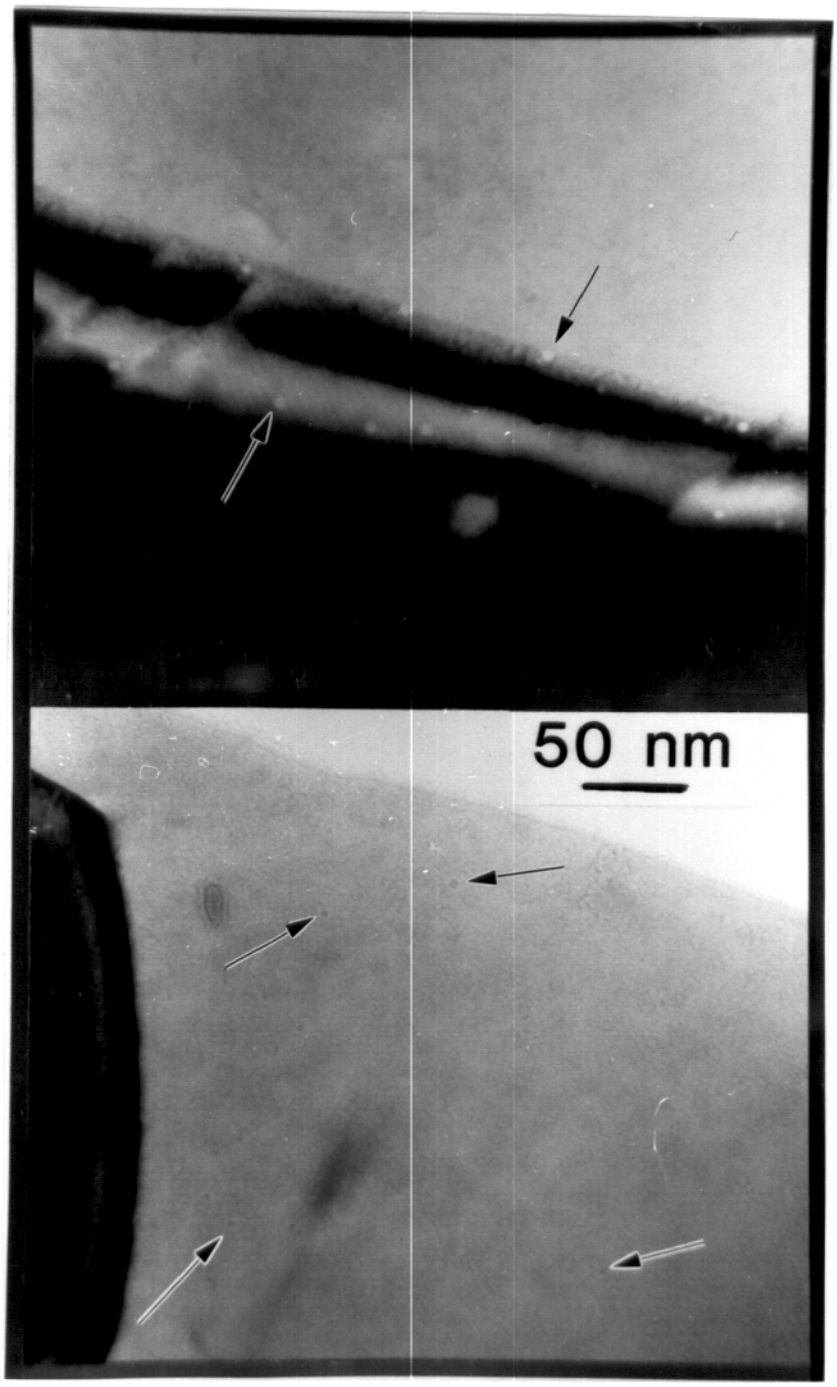

Figure 6.12. TEM micrographs of L9 showing small bubbles which formed after ion-irradiation at 550°C to 40 dpa.

Discussion

Ion irradiation did not lead to any phase changes in L9, although some phase instabilities developed during neutron irradiation. If the two experiments (ion versus neutron irradiation) are compared, it can be seen that not only was the damage rate different, but the thermal treatments which the samples received were not the same. The samples which had the least damage after the neutron irradiations (approximately 15 dpa), were still subjected to substantial thermal effects as it took approximately 5000 hours to reach this displacement level. In the ion irradiations, the samples irradiated to the highest displacement level were only at temperature for approximately five hours.

In the sample neutron irradiated at 600°C, an area with large amounts of austenite was present (Figure 6.2, p. 77). As these features were also seen in a few of the aged samples, and because some areas of the 600°C irradiated samples were austenite free, it can be concluded that the austenite was probably present prior to irradiation. This conclusion is also supported by the lack of austenite formation in the sample ion irradiated at 650°C. No austenite was found in these samples, and there was no evidence that during the irradiation new austenite had formed and reverted to martensite. The structure was one of over-annealed martensite (Figure 6.8, p. 85). This indicates that at 600°C and 650°C, the steel is very stable in an irradiation environment.

Neutron irradiation at 420°C led to the formation of what were probably α' precipitates (Figure 6.5, p. 80). The precipitates are coherent, Cr rich particles, and their structure is bcc with a lattice parameter very close to that of the Fe-rich matrix. The formation of α' has been demonstrated in other irradiated 12% Cr steels (1), and in aged 14-28% Cr steels (2). The Fe-Cr system shows a metastable miscibility gap which is calculated to close at approximately 630°C (3). Neutron irradiation of L9 at 420°C has led to the formation of this metastable phase at a temperature where it did not form when L9 was simply aged. The formation of α' is not desirable, as its presence can cause embrittlement (2), and therefore irradiation of L9 at 420°C can have undesirable consequences.

Unlike the L9 alloy aged at 420°C, no chi was found in the 420°C neutron irradiated samples. This indicates that irradiation at 420°C inhibited chi phase formation because the time in the reactor was at least as long as the time it took for chi to form in the aged samples. However, when L9 was neutron irradiated at 520°C, large amounts of the brittle Fe-Cr-Mn-W chi phase formed. It took approximately 5000 hours to reach 14 dpa, but the sample aged at 520°C for 5000 hours had much less chi present indicating that the irradiation led to an increase in the amount of chi which formed. At 420°C, the amount of chi phase may be less due to irradiation dissolution, while at 520°C, diffusion of solute back to the chi phase may have been rapid enough to allow the chi phase to remain stable in spite of the irradiation. The increase in the amount of chi present in the 520°C neutron irradiated sample relative to the 520°C aged sample appears to be due to radiation induced

segregation. This is evidenced by the chi grains lying mostly at lath boundaries in the neutron irradiated samples (Figure 8.3, p. 78), while in the aged samples, chi was seen at both lath boundaries and within the martensite laths. In the ion irradiated samples, chi may not have been present due to the much shorter time for which the steel was held at the high temperature. In addition to the shorter thermal treatment, the dissolution of phases by radiation can be enhanced with a higher displacement rate because the rate of particle loss by the solute will be increased. The large amounts of chi which formed in L9 when it was both aged and neutron irradiated means that the steel may not be useful as chi phase is very brittle.

It is interesting to compare the phase stability of irradiated L9 with that of other irradiated 12% chromium martensitic steels. As mentioned earlier, phase instabilities are quite common in these complex ferritic alloys after irradiation. Table 6.1 summarizes the precipitate evolution of some of these steels during irradiation (4). In the unirradiated Ni-stabilized steels, there are a number of precipitates present that were not seen in L9. Although $M_{23}C_6$ is the equilibrium carbide expected in all of these steels (5), other precipitates are also found. In the standard Ni-stabilized martensitic stainless steels, M_2X, and MX are sometimes present in addition to $M_{23}C_6$. Both ion irradiation (4), and neutron irradiation (1) have led to the dissolution of M_2X. There was perhaps some dissolution of $M_{23}C_6$ in L9 after ion irradiation at 650°C, but it was very stable during neutron irradiation (Figure 6.1, p. 77). It was even present inside many of the chi grains which formed at 520°C (Figure 6.4, p. 79). The carbide stability in L9 can be attributed to the more

Table 6.1. Precipitate Evolution of Martensitic Stainless Steels During Irradiation

Alloy	Irradiation Dose	Temp. (°C)	Precipitate before irradiation	Precipitate after irradiation	Ref.
HT-9*	36 dpa (neutron)	300, 400, 500, 600	$M_{23}C_6$, MC	$M_{23}C_6$, MC	6
HT-9*	39 and 75 dpa (neutron)	300, 400 to 650	$M_{23}C_6$	χ, G, α', $M_{23}C_6$	7
HT-9	up to 200 dpa (14 MeV Fe^+)	300, 400, 500, 600	MX, M_2X, $M_{23}C_6$	MX, χ, $M_{23}C_6$	4
CRM-12#	30 dpa (neutron)	380, 420, 460, 615	NbC, M_2X, $M_{23}C_6$	χ, Laves, MX[a], M_6C, $M_{23}C_6$, α'	1
FV448#	30 dpa (neutron)	380, 420, 460, 615	NbC, M_2X, $M_{23}C_6$	Laves, α' M_2X[a], σ, χ, $M_{23}C_6$, M_6X	1
FI#	30 dpa (neutron)	380, 420, 460, 615	$M_{23}C_6$, M_2X[b]	M_6X, χ, $M_{23}C_6$, α'	1
L9	various (neutron and ion)	420 to 650	$M_{23}C_6$	$M_{23}C_6$, χ, α'	this work

* Composition in Table 3.1, # Compostion in table 5.1, [a] some dissolution occured after irradiation, [b] irradiation totally dissolved phase.

rapid formation of its equilibrium carbide than occurs in the Ni-stabilized martensitic stainless steels, so that irradiation is not as likely to change the precipitate structure.

The other phases which do not form in L9 but which can form in irradiated Ni-stabilized martensitic steels are G-phase, a nickel silicide (7) and M_6C (1), a carbide which usually contains Ni (1, 8). There were no similar manganese phases which formed in L9 indicating that Mn does not simply substitute for Ni in the precipitates. As noted earlier, α' can form in both Ni-stabilized martensitic stainless steels and in L9.

Chi phase has been shown to form in both ion irradiated (4) and neutron irradiated Ni-stabilized martensitic stainless steels (1, 7, 9). But in the Ni-stabilized martensitic stainless steels, the amount and size of the chi which forms (usually < 100 nm in size) is much lower than that which formed in L9, so that increasing the manganese content in L9 apparantly increased the amount of chi which formed during neutron irradiation at 520°C. This increase is not surprising in light of the aging results which showed it to be a stable phase in L9 (Figure 5.18, p. 61), while in the Ni-stabilized martensitic stainless steels, chi phase is not stable.

The alloying changes in L9 did not degrade its swelling resistance. Even at a temperature close to that of the peak swelling temperatures in ferritics (420°C-neutron irradiation, 550°C-ion irradiation), with a dose as high as 114 dpa, there were few voids found. Recent results on HT-9 which was irradiated in FFTF to 114 dpa showed a higher swelling than L9 (10). Co-irradiation with Fe^{++} and He^{+} ions led to the formation of small He

bubbles at 18 and 40 dpa, but their density was still very low. At 6 dpa, no bubbles were seen. This swelling resistance was not surprising because although L9 does have a high Mn content, it is still a fine grained bcc alloy with a high dislocation density.

The number of loops which formed in L9 was much lower than that found in other 12% Cr ferritic steels which were neutron irradiated at 420°C. (1). Even at 114 dpa, there were very few loops. Loops were found in the ion irradiated samples, but at 550°C and 650°C, there were few and their distribution was uneven. At 450°C, their size was very small.

The void swelling and loop formation resistance of L9 is probably not due to the increased manganese content as another 6.5% Mn martensitic stainless steel which was irradiated swelled more on the order of HT-9 (11). The difference instead may simply be due to the pre-irradiation heat treatment, which changes the initial dislocation density and lath size and shape. A recent study on HT-9 which had been given two different normalizing and tempering treatments, reported a variation in the swelling and irradiation induced dislocation density of the alloy (10). It was found that the irradiation induced dislocation structure and swelling was somewhat higher in HT-9 when the alloy started with a lower dislocation density. The variation in the heat treatments apparently did not change the phase stability during irradiation.

Although the neutron and ion irradiation phase stability results were quite different, there were some similarities in the results of the ion and neutron irradiations. Both experiments led to a reduction of the dislocation

density, and to enhanced subgrain formation in L9. The void swelling results were also comparable between the two experiments, with the expected exception of bubble formation in the 550°C ion irradiated samples where helium was co-implanted with the Fe ions.

References for Chapter 6

1. E.A. Little and L.P. Stoter, *Effects of Radiation on Materials: Eleventh Conference ASTM STP 782* , H.R. Brager and J.S. Perrin, Eds., ASTM (1982) 207.

2. R.M. Fisher, E.J. Dulis, and K.G. Carroll, *Trans. AIME* 197 (1953) 690.

3. P. J. Spenser and J.C. Counsell, *Z. Metallkd.,* 64 (1973) 662.

4. J. J. Kai, Ph.D. Thesis, University of Wisconsin-Madison, (1986).

5. R. Smith, *ISI Spec. Rept.* No. 64 (1959) 307.

6. J.M. Vitek and R. L. Klueh, *Met. Trans.*, 14A (1983) 1047

7. D. S. Gelles and L.E. Thomas in *Proceedings for the Topical Conference on Ferritic Alloys for Use in Nuclear Energy Technologies* Edited by J. W. Davis and D.J. Michel, Snowbird Utah (1983) 559.

8. The Bristol Group under the direction of John Steeds, *Convergent Beam Electron Diffraction of Alloy Phases,* Adam Hilger Ltd. Bristol and Boston, (1984) 47.

9. D.S. Gelles, *J. Nucl. Mater.* 103&104 (1981) 975.

10. D.S. Gelles, and A. Kohyama in *Fusion Reactor Materials Semiannual Progress Report for Period Ending March 31, 1989* DOE/ER-0313/6 193.

11. D.S. Gelles, "Effects of Irradiation on Low Activation Ferritic Alloys, A Review", presented at the *International Symposium: Reduced Activation Alloys for Fusion Service* (1988) Andover, Mass.

Chapter 7: Conclusions and Suggestions for Future Work:

The alloy L9 was designed to be a martensitic steel which would behave similarly to other 12% chromium martensitic steels, with the exception that it would have reduced long-life radioactivity. This study has shown that in some areas the alloy met its goals, while in others it did not. On the success side, air cooling of the steel led to the desired martensitic structure. Only 3% retained austenite remained, and delta ferrite was not commonly found. The A_{c1} for the steel lay above 700°C (between 700°C and 800°C) as was desired, and the carbide structure was stable in both a thermal and irradiation environment. If the steel was tempered at temperatures above 500°C, then only $M_{23}C_6$ formed. The addition of Mn also did not change the swelling resistance of the steel. Irradiation at the peak swelling temperatures with both neutrons and ions+helium did not cause substantial swelling. In fact, the steel showed less swelling than HT-9 after it was irradiated in FFTF to 114 dpa (1).

The major problem which the steel showed was a tendency to form large amounts of an Fe-Cr-Mn-W chi phase. This instability means that this steel will probably not be useful in a fusion environment. The literature and this study have shown that the Fe-Cr-Mn system can form chi phase at compositions where it is not expected, although its formation does not appear to be easy. This is born out by the following observations. 1) In simple Fe-Cr-Mn alloys, where W and/or Mo are not present, no report in the literature was found of chi phase formation. 2) In more complicated Fe-Cr-Mn alloys,

where W and/or Mo are present, it does not always form, even after long aging (2,3). 3) In austenitic alloys it tends to form at grain boundaries (4); in bcc steels chi tends to form with an orientation relationship to the matrix, or at boundaries (this work). 4) In the steel of this study, chi phase formation was very sluggish. So perhaps with careful alloying, chi phase formation can be eliminated. In the 12% Cr steels, Mn has been shown to enhance chi phase formation in both W (this work) and Mo steels (5). Perhaps if the W and Mo contents were eliminated or decreased, chi phase formation would decrease. It also might be possible to decrease or eliminate chi phase formation in the 12%Cr-martensitic steels by using 0.2%C, so that less additional Mn would be needed to stabilize the martensitic structure. With lower Mn contents, perhaps W could still be used for tempering resistance.

The Fe-Cr-Ni austenitic and martensitic stainless steels have been studied for many years so that there is extensive information available concerning their phase stability. There is much less information available for the Fe-Cr-Mn alloys. This study indicates that the Fe-Cr-Mn alloys may need to be heat-treated for rather long times to test their phase stability. If this study had simply relied on short time anneals and ion irradiations, it would have been concluded that L9 appeared to be a very successful alloy design. Both alloys investigated in this study did not show phase instability until they were aged for at least 1000 hours. The simple Fe-Cr-Mn alloy did not transform until somewhere between 2000 and 5000 hours, and the amount of chi which formed in L9 after 1000 hours was still very low.

References for Chapter 7

1. D.S. Gelles and Akira Kohyama in *Fusion Reactor Materials Semiannual Progress Report for Period Ending March 31, 1989* DOE/ER-0313/6 193.

2. A.H. Bott, F.B. Pickering, G.J. Butterworth, *J. Nucl. Mat.* 141-143 (1986) 1088.

3. P.J. Maziasz and R.L. Klueh presented in the *14th Int. Symp. on Effects of Radiation on Materials* held in Andover MA June 27-29 1988.

4. J. M. McCarthy in *Fusion Reactor Materials Semiannual Progress Report for Period Ending March 31, 1989* DOE/ER-0313/6 p. 103.

5. A. Kohyama and D.S. Gelles *Annual Progress Report for Fusion Year 1987.*